J Mater Sci (2013) 48:6849–6877
DOI 10.1007/s10853-013-7541-0

REVIEW

One-dimensional ZnO nanostructures: fabrication, optoelectronic properties, and device applications

Debashis Panda · Tseung-Yuen Tseng

Received: 17 March 2013 / Accepted: 14 June 2013 / Published online: 26 June 2013

Abstract One-dimensional (1D) zinc oxide (ZnO) nanostructures have been extensively and intensively studied for several decades not only for their extraordinary chemical and physical properties, but also for their current and future different electronic and optoelectronic device applications. This review provides a brief overview of the progress of different synthesis methods and applications of 1D-ZnO nanostructures. Morphology of ZnO nanostructures grown by various methods and progress in the optical properties are briefly described. Using low-temperature photoluminescence (LTPL) study, detailed informations about the defect states and impurity of such nanostructures are reported. Improvement of field emission properties by modifying the edge of 1D-ZnO nanostructures is briefly discussed. Applications such as different sensors, field effect transistor, light-emitting diodes (LEDs), and photodetector are briefly reviewed. ZnO has large exciton binding energy (60 meV) and wide band gap (3.37 eV), which could lead to lasing action based on exciton recombination. As semiconductor devices are being aggressively scaled down, ZnO 1D nanostructures based resistive switching (RS) memory (resistance random access memory) is very attractive for nonvolatile memory applications. Switching properties and mechanisms of Ga-doped and undoped ZnO nanorods/NWs are briefly discussed. The present paper reviews the recent activities of the growth and applications of various 1D-ZnO nanostructures for sensor, LED, photodetector, laser, and RS memory devices.

D. Panda · T.-Y. Tseng (✉)
Department of Electronics Engineering, and Institute of Electronics, National Chiao Tung University, Hsinchu 30010, Taiwan
e-mail: tseng@cc.nctu.edu.tw

Introduction

There has been a tremendous interest, admiration in nanostructured zinc oxide (ZnO), a II–VI semiconductor, for its various potential applications in optoelectronics devices and other applications owing to its wide direct band gap ($E_g = 3.3$ eV at 300 K) and also a relatively large exciton binding energy (60 meV) [1–5], which could lead to lasing action based on excitonic recombination at room temperature. It is assumed that ZnO may replace another wide band gap semiconductor GaN ($E_g = 3.4$ eV at 300 K) for some optoelectronic applications, which is widely used for green, blue–ultraviolet (UV), and white light-emitting devices fabrication. It can be potentially used for making low-cost ZnO-based devices for its simpler fabrication process. It has high thermal and mechanical stabilities due to high melting point (1975 °C) and large cohesive energy of 1.89 eV. Owing to the above advantageous parameters, ZnO exhibits near UV emission, conductivity, transparency, and resistance to high-temperature electronic degradation. The optical properties of ZnO make it one of the most promising materials for photonic devices in the UV range. ZnO has been investigated in the semiconductor field dated back to 1935 by Bunn [6]. Lattice parameter, and vibrational properties with Raman scattering in 1966 by Damen et al. [7] and growth by chemical-vapor transport (CVT) method in 1970 by Galli and Coker [8] have been carried out in ZnO. In terms of optoelectronic device applications, Au Schottky barriers and Al/Au Ohmic contacts have been proposed by Mead [9] and Brillson [10], respectively.

Advantages of ZnO thin film

Although the research work on ZnO thin film has been started during 1930s [6], the interest faded away during

1980s due to the difficulty in doping; both in n- and p-type. Doping is a prerequisite for optoelectronic device applications, partially because the significance moved to structures of reduced dimensionality, like quantum wells. The research highlighted on ZnO at that time was basically on bulk samples covering topics like growth, doping, transport, deep centers, band structure, excitons, bulk- and surface-polaritons, luminescence, high excitation or many-particle effects, and lasing. Early research work on ZnO is briefly reviewed in different papers [11–14].

ZnO has played an important role in the fabrication of transparent thin film transistors (TFT) and achieved extra functions such as photodetections using ZnO channel. ZnO has a number of basic benefits over other wide band gap semiconductors, GaN and SiC, such as free excitonic binding energy is much higher than that of GaN (21–25 meV) and amenability to wet chemical etching. Recent years ZnO films were considered as transparent conducting oxide due to their good electrical and optical properties in combination with abundance in nature, large band gap, optical transmittance (>80 %) in visible region, and the absence of toxicity [15]. ZnO was also considered as a promising candidate for bio-sensors [16, 17], having exceptional advantages including chemical stability, electrochemical activity, nontoxicity, and high electron communication features. It preferentially crystallizes in the hexagonal wurtzite-type crystal structure [18–20]. Except the optoelectronic potential of ZnO [21–23], it possesses piezoelectric property [24], biocompatible and bio-safe properties [25–28], and ferromagnetic properties with prospective for spintronics devices [28–30]. Due to the advantageous optoelectronic properties, ZnO nanostructured thin film can be used in light-emitting diode (LED), photodetector, laser diode, and solar cell. The ZnO is also a promising candidate for nonvolatile resistive switching (RS) memory devices in recent years.

Classifications of ZnO nanostructures

ZnO has probably the richest variety of different nanostructures in the field of semiconductor technology [31, 32]. Its range includes highly ordered nanowires (NWs) [33–35], nanorods (NRs) [36–38], nanobelts [39, 40], nanotubes [41, 42], nanohelixes [43, 44], nanorings [45, 46], etc., as shown in Fig. 1. The early growth of bulk ZnO crystals can be achieved using different techniques, such as thermal evaporation [47–50], metal–organic vapor-phase epitaxy (MOVPE) [51, 52], laser ablation [53, 54], aqueous solution synthesis [55–58], and electrodeposition [59, 60].

In the last few decades, especially since the nanotechnology initiative led by the United States, investigation of one-dimensional (1D) nanomaterials including NWs, nanotubes, nanofibers, NRs, and nanobelts have attracted much attention in nanoscience and nanotechnology [20, 61]. By reducing size, novel mechanical, electrical, chemical, and optical properties are introduced. The 1D nanostructures offer ideal structures for studying transport processes of the one-dimensionally confined objects, investigating related fundamental phenomena, and developing the next-generation high-performance nanodevices [62]. In comparison with 0D and 2D nanomaterials, 1D nanomaterials offer an enhanced model system for investigating the dependence of electrical and optoelectronic properties on size reduction and dimensionality. NWs and NRs are a new class of quasi 1D nanomaterials that have been attracting great research interest in the past few years. Their superior electrical, mechanical, optical, and thermal properties permit them to be used as primary building blocks for nanoscale science and technology in the fields of electronic devices [63–65].

In this review, we first discuss the growth of various ZnO 1D nanostructures. A brief appraisal is made on the status of the various optical applications of ZnO-NWs, NRs, and nanotubes. Then a comprehensive review on the recent progress is made in terms of the use of ZnO 1D nanostructures as a field emitter. The potential of the application in various sensor devices are illustrated. Prospective photoluminescence properties of 1D-ZnO nanostructures are reviewed. Applications of these structures for optoelectronic and photovoltaic devices are presented. Finally, the potential for emerging nonvolatile RS memory device is described.

Growth and morphologies of 1D-ZnO nanostructures

In this section, we discuss about the various growth methods and morphologies of 1D-ZnO nanostructures. The growth and morphologies of doped and core–shell structures of 1D-ZnO nanostructures are not reviewed.

Chemical growth

In 1999, Pauporte and Lincot [66] first reported the fabrication of electrodeposited ZnO-NRs on gallium nitride (GaN) substrate, having an average diameter of a few hundred nanometers. Later Levy-Clement et al. [67] and Tena-Zaera et al. [68] prepared solar cells using electrodeposited n-type ZnO-NWs (length $>$ 100 nm and wide $\sim$100–300 nm) on fluorine-doped tin oxide (FTO) substrates. Guo et al. [69] reported the growth of well-aligned narrow ZnO nanorod (diameter 15–30 nm) arrays (ZNAs) by using a potentiostatic electrodeposition method. After then, several groups demonstrated the growth of ZnO 1D nanostructures by chemical methods [70–75].

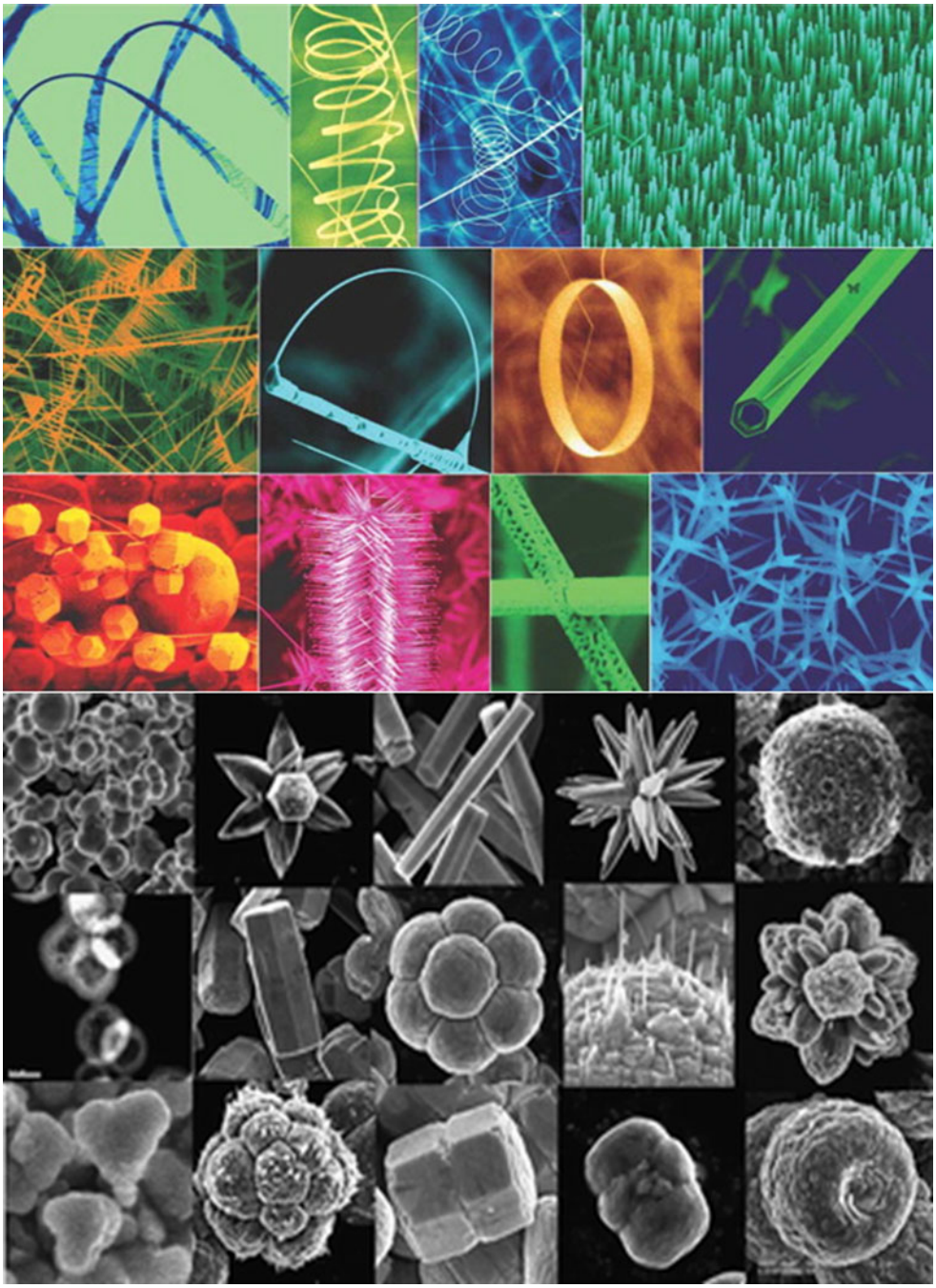

Fig. 1 SEM images of various ZnO nanostructures [31, 32]

Yang et al. [76] reported the fabrication of crystalline well-aligned ZNAs with various diameters on Si(001) substrates by two-step chemical bath deposition (CBD) method. Formation of ZnO nanotips from the as-deposited chemically grown ZnO-NRs by using combination of chemical and plasma etching process was reported by us [77, 78]. Plasma etching process was employed followed by the chemical etching to the obtained sharper ZnO nanotips with a variety of tip angles. Figure 2a shows that ZnO acute nanotips are formed (inset of Fig. 2a) after plasma treatment. Smaller tip angle was obtained by using the combination of chemical and plasma etching. Figure 2b shows the SEM image of the nanotips obtained after 2-h chemical etching followed by plasma treatment (inset of Fig. 2b). Tip angle and dimension of the NRs after two-step etching process are confirmed from the HRTEM, as shown in Fig. 3. The preferred [001] directional growth of the ZnO-NRs with clear lattice fringes indicates that the

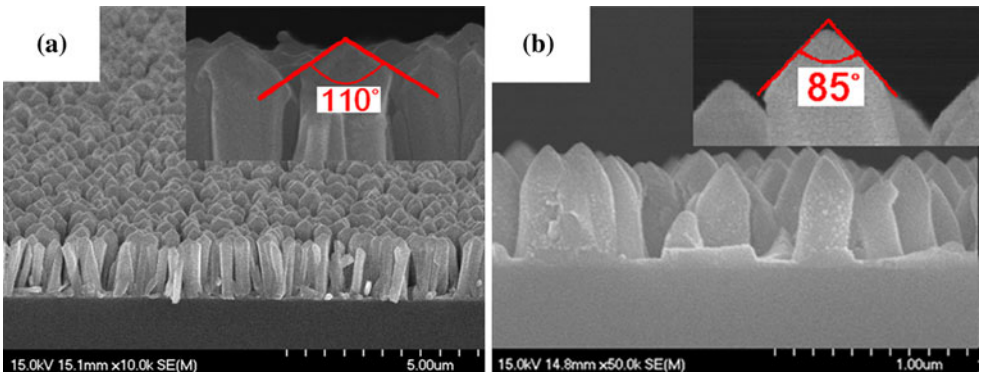

Fig. 2 Typical SEM images of the ZnO-NRs grown by chemical method after **a** plasma and **b** two-step etching [78]

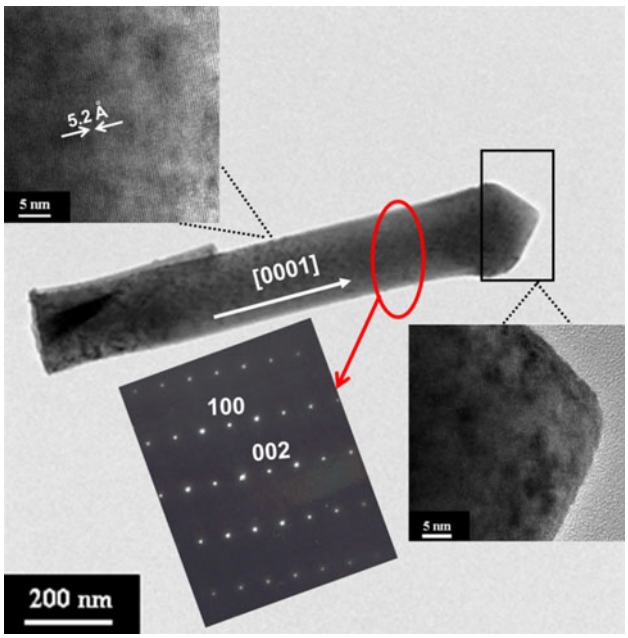

Fig. 3 TEM image of the chemically grown single ZnO-NR after plasma etching, the *insets* show the corresponding SAED pattern and high-resolution TEM image [78]

interplanar spacing of the ZnO is 5.2 Å (inset in Fig. 3). ZnO-NRs field emitters were also prepared by us by etching the NRs with oxygen plasma for various times [73].

Yao et al. [78] also fabricated nanopagoda by surface modifications by chemical solutions of chemically grown NRs followed by plasma treatment, as shown in Fig. 4a. Tip width and base diameter of the laminated nanopagodas are varied from 30–50 nm to 500–650 nm (inset of Fig. 4a), respectively, indicating that after oxygen plasma treatment for 30 s, ZnO nanotip emitters are sharpened and exhibit a tip angle approximately 20°, as shown in Fig. 4b. Smooth surface edge area of the emitters (Fig. 4b) indicates that oxygen plasma treatment is a fast and powerful nanoscale surface modification method [78]. Figure 5 indicates the typical high-resolution cross-sectional TEM image of the nanopagoda and nanotip emitters. Right inset of the Fig. 5 shows the nanostructures grown in the [100] direction.

Metal–organic chemical vapor deposition growth

The most widespread method for the growth of ZnO nanostructures is metal–organic chemical vapor deposition (MOCVD) [79–82]. Kim et al. [81] demonstrated ZnO-NWs with diameters ranging from 20 to 60 nm and lengths in the range 5–15 μm were synthesized by MOCVD, assisted by colloidal Au nanoparticles dispersed on SiO_2/Si substrates. Normally, catalyst is not mandatory in MOCVD method, resulting in that the purity of ZnO is high because that there was no impurities resulting from any catalyst [82]. One important advantage of MOCVD grown NWs is the prospect of growing the film on top of the NWs which permits fabrication of devices without using any insulating layers [83, 84]. ZnO quantum dots were observed using nitrogen dioxide as the oxygen source [85], whereas 1D-ZnO was achieved when molecular oxygen was used as the oxygen source [86]. Large nanosized ZnO islands were achieved by MOCVD by using nitrous oxide as an oxygen source [87].

Park et al. [51] fabricated [001]-oriented ZnO-NWs on sapphire substrate using MOCVD method without using any catalyst. While MOCVD is considered as an appropriate technique for the development of highly oriented arrays of NWs with demonstrated good in-plane alignment on the substrate surface [51, 88, 89], its capability is somewhat limited in terms of mass production. Lee et al. [90] investigated the prospect of growing highly crystalline and high optical quality ZnO-NWs without using any catalysts. The selective growth of self-assembled uniform and orientated ZnO nanotips on various substrates such as Al_2O_3, epitaxial GaN, fused silica, and SiO_2/Si substrates using MOCVD was proposed by Muthukumar et al. [86]. Montenegro et al. [91] investigated the morphology transitions (NRs–nanowalls and NRs–nanotubes layer) induced

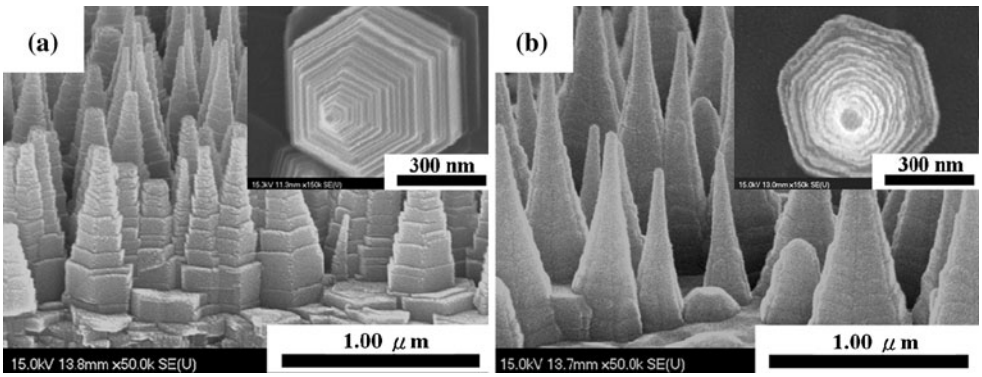

Fig. 4 Typical FESEM images of chemically grown **a** nanopagoda and **b** nanotip emitters; *inset* shows their top view [78]

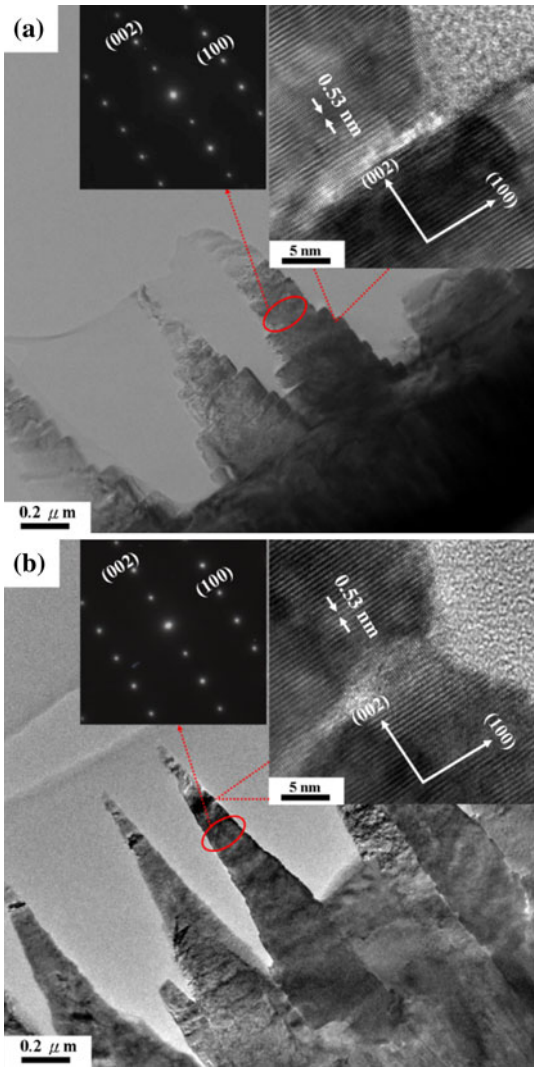

Fig. 5 Cross-sectional TEM images with corresponding SAED patterns and HRTEM images of chemically grown ZnO **a** nanopagoda and **b** nanotip emitters [78]

in the growth of ZnO nanostructures by MOCVD on c-sapphire. Modes of the epitaxial growth of ZnO-NWs, nanoneedle, and nanotips were also reported [82, 92–95]. Yin et al. [96] reported the fabrication of ZnO quantum rods having diameters ~2 nm and lengths ~40–50 nm. Gu et al. [97] prepared ZnO-NRs with radius of 1.1 ± 0.1 nm, which is less than the bulk exciton Bohr radius of ZnO ($a_B \sim 2.34$ nm). Gargas et al. [98] also demonstrated ZNAs (~1520 μm length and 100 nm diameter) on R-plane sapphire substrates using CVT method.

Vapor-phase transport growth

Among the various methods of ZnO 1D nanostructures fabrication, the simplest, oldest and still widely used method is vapor-phase transport (VLS) [99–102]. Using this convenient method, high-quality pure hexagonal ZnO needles of few millimeters in diameter and several centimeters in length can be achieved [100]. Morphology of 1D-ZnO nanostructures not only depended on the growth method but also on different experimental parameters such as substrate, process temperature, carrier gas, and dopant [102]. Grabowska et al. [102] demonstrated that NW growth on a-plane sapphire is quite well aligned along vertical direction; growth on SiO_2 is poorly aligned.

Huang et al. [3, 103] fabricated highly oriented ZnO-NWs using VLS process via catalyzed epitaxial crystal growth. Typical SEM images of NW arrays grown on sapphire (110) substrates with different patterned Au thin films are shown in Fig. 6. Figure 6a, b shows the low-resolution view of the grown NWs. No growth of the NWs is observed in region without gold layer, as shown in Fig. 6c. A side and top view of well-faced aligned NWs are shown in Fig. 6d and e, respectively. Diameters of these wires range from 20 to 150 nm, whereas more than 95 % of them have diameters of 70–100 nm. HRTEM image of an individual ZnO-NW is shown in Fig. 6f, showing (0001) growth direction of the NWs [3].

ZnO-NWs grown by VLS method on Si(001) substrate using Cu catalyst was reported by us [104]. The typical growth of NWs is shown in Fig. 7. Thicker Cu-coated

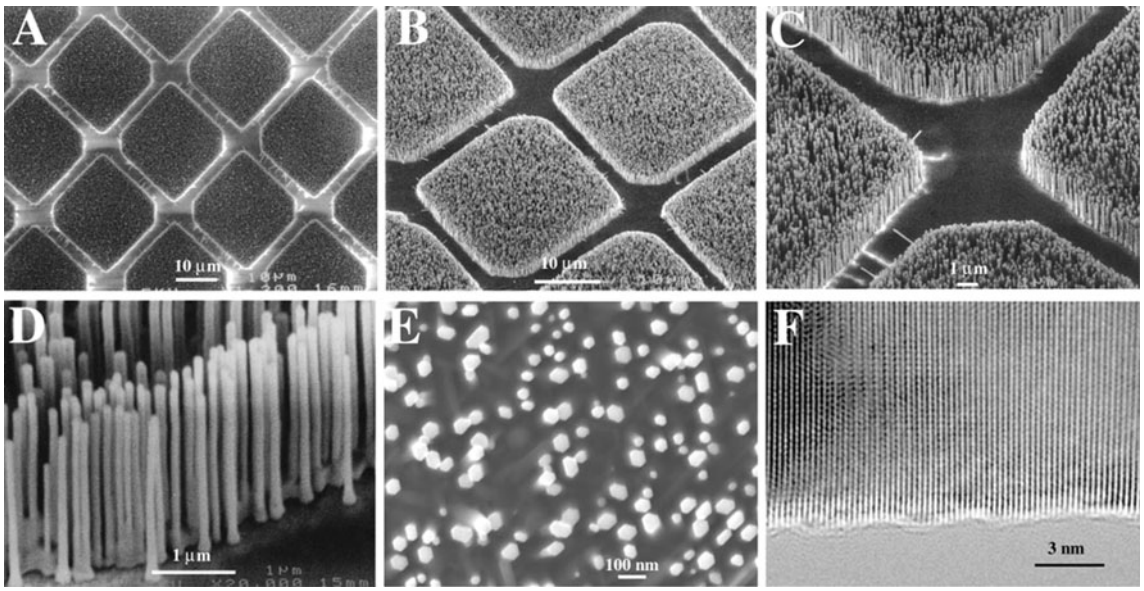

Fig. 6 **a–e** SEM images of ZnO-NW arrays grown on sapphire substrates by VLS method. A top view of the well-faceted hexagonal NW tips is shown in **e**. **f** High-resolution TEM image of an individual ZnO-NW showing its (0001) growth direction [3]

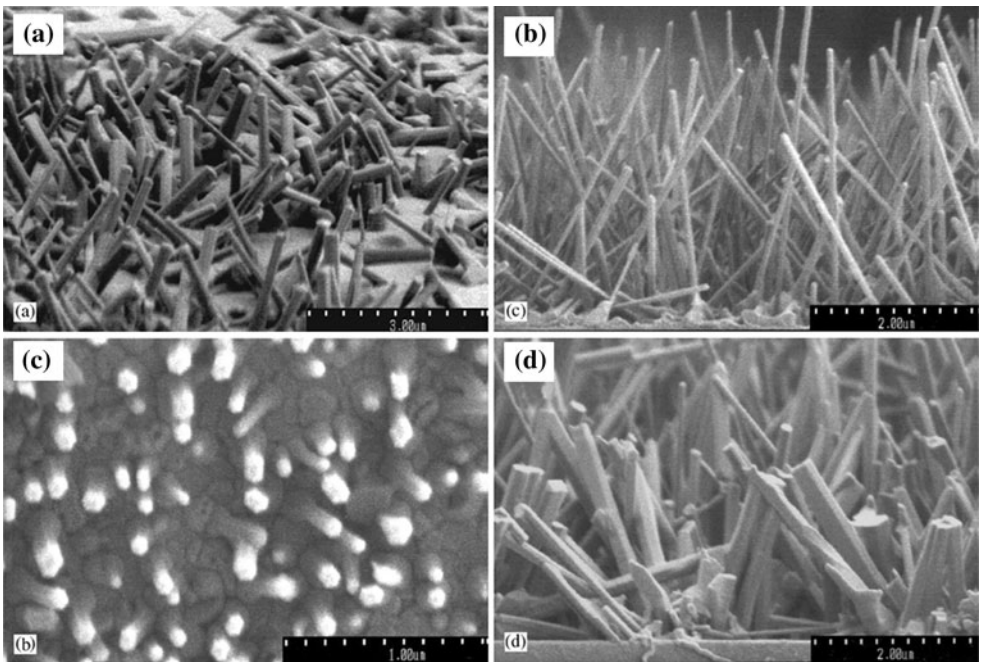

Fig. 7 FESEM images of ZnO-NWs grown by VLS method on Si(001) using Cu catalyst: **a** tilted 45° view, **b** top view, **c** growth on 7-nm-thick copper film, **d** growth on 15-nm-thick copper film [104]

Si(001) substrate produced larger diameter ZnO-NWs. Figure 7c, d demonstrates the formation of different diameters of ZnO-NWs by using different thicknesses of copper films. Top of the ZnO-NWs with Cu tips was quite smooth and hexagonal (Fig. 7b). Growth of ZnO-NWs by VLS method using Sn catalyst was reported by Yang and Wang [105], as shown in Fig. 8. Growth of ZnO-NRs on different crystalline as well as amorphous substrates by VLS method using Au catalyst was reported [106, 107]. Saunders et al. [108] modeled that the length of the ZnO-NWs, grown by VLS method, increases with decreasing NW radii. Among the several advantages, the main disadvantage of this method is that the deposition needs to be performed at high temperature. This is not suitable for some applications such as deposition in polymer substrate for flexible electronic device applications.

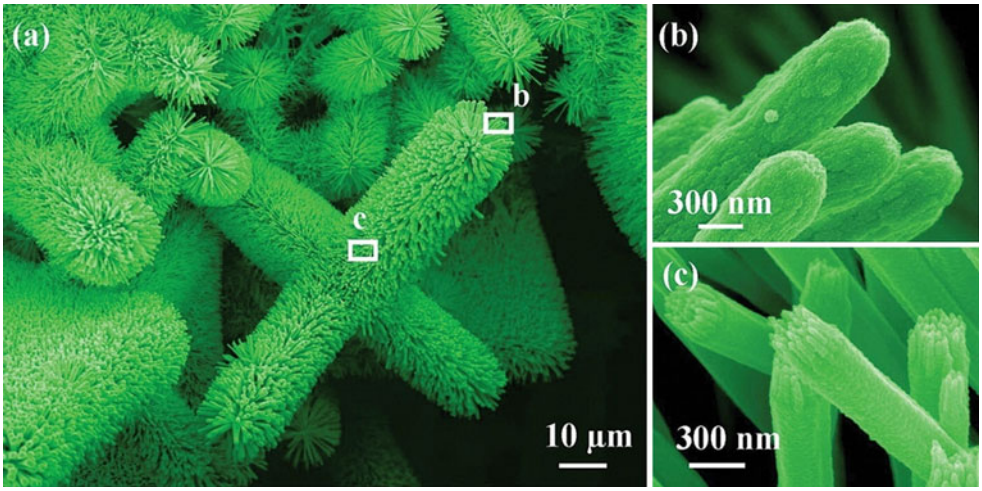

Fig. 8 **a** Uniaxial fuzzy VLS grown ZnO-NW clusters from a higher temperature region. **b**, **c** Enlarged images of NWs from white *squared* area in **a** [105]

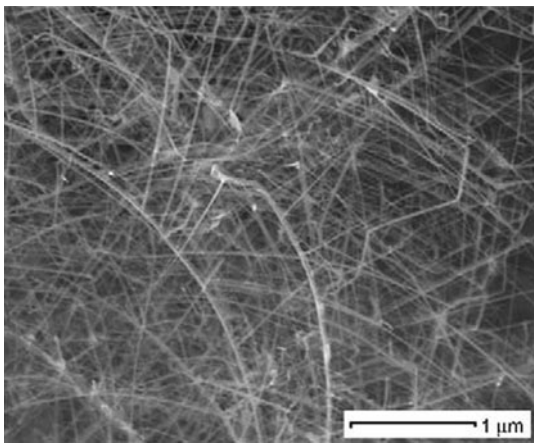

Fig. 9 FESEM images of the as-deposited rf sputtered ZnO-NWs on copper substrate [110]

Growth by physical method

Numerous groups reported the growth of 1D-ZnO nanostructures by physical methods [109–117]. Hung et al. [109] and Choopun et al. [110] fabricated ZnO-NWs by rf magnetron sputtering. The ZnO-NWs have a thickness and width of about 10 and 50 nm, respectively, as shown in Fig. 9. A Zn/ZnO nanocable fabricated by thermal oxidation of Zn-NWs on p-Si(001) grown by rf magnetron sputtering was reported by Kim et al. [111]. Heo et al. [112] demonstrated the site-selective growth of ZnO-NRs on p-Si(001) (diameters 15–40 nm; length 1 mm) using catalysis-driven molecular beam epitaxy (MBE). There were several reports that described the growth of ZnO-NRs by MBE [113, 114].

Various 1D-ZnO nanostructures such as NWs, nanoribbons, and needle-like rods grown by thermal evaporation of graphite-mixed ZnO (1:1) powders are shown in Fig. 10 [115]. Three kinds of morphologies namely needle-like rods (Fig. 10a), nanoribbons (Fig. 10b), and NWs (Fig. 10c) are observed. Diameters of ZnO-NWs were temperature dependent and low growth temperatures resulted in small diameters of ZnO-NWs [115]. Effect of formation temperatures on the morphologies is schematically shown in Fig. 10d. Choopun et al. [117] reported the growth of self-assembled ZnO-NRs on c-plane sapphire by pulsed laser deposition (PLD). Crystalline ZnO-NWs on Au-coated sapphires and p-Si(001) substrate were grown by the PLD method using a femtosecond (fs) laser ablation source (Fig. 11) [118].

Fabrication on patterned substrates

Template-assisted growth of 1D nanostructures especially fabrication of tubular structures with monodisperse diameters and lengths is an elegant synthesis method [119–121]. Anodic alumina membranes (AAM) templates have been mostly used for synthesis of such 1D nanostructures [121–123]. Fabrication of ZnO nanotube arrays, as shown in Fig. 12, by electrochemical deposition using AAM was first reported by Li et al. [124]. The main disadvantages of this technique are poor cohesion, complex synthesis steps, and ease in cracking. Fully controlled growth over centimeter-scale area of vertical ZnO-NR/NW arrays using polystyrene (PS) sphere templates and electrochemical deposition method was reported [125, 126].

Hydrothermal method

Hydrothermal method is another popular technique to grow various nanostructures [56, 127–130]. Tam et al. [128]

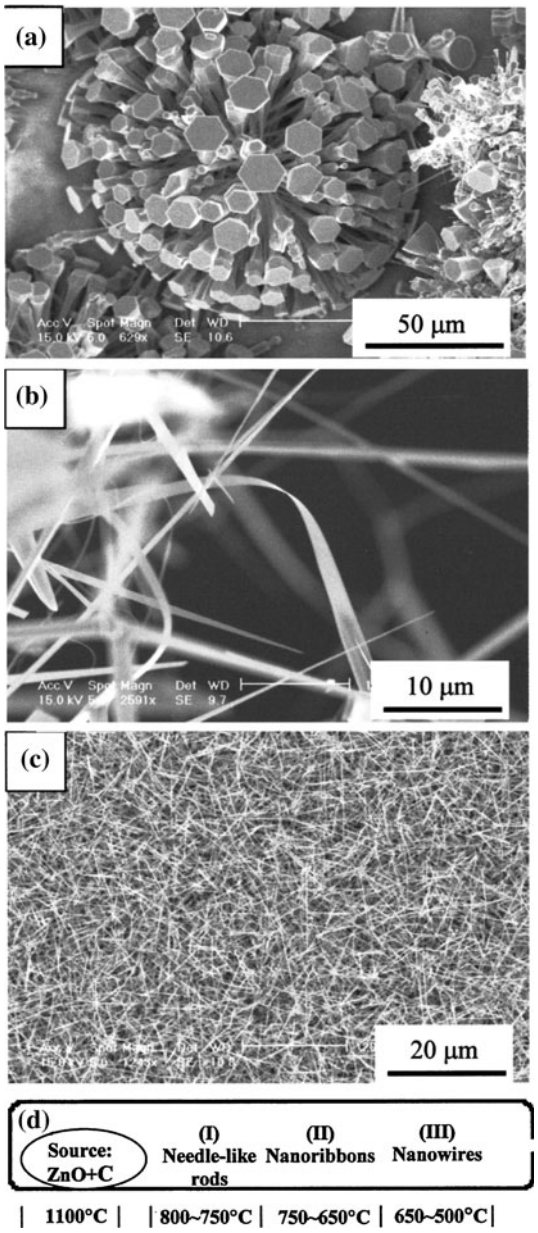

Fig. 10 SEM images showing the three typical morphologies of the as-deposited evaporated ZnO products: **a** needle-like rods, **b** nanoribbons, **c** NWs, and **d** their corresponding growing site temperatures [115]

reported the growth of well-aligned ZnO-NRs on p-Si(001) substrate, as shown in Fig. 13. Liu and Zeng [56] prepared monodisperse highly crystalline *c*-axis-oriented ZnO-NRs having diameter of ~50 nm with large aspect ratios. Chen and Wu [130] briefly reported nucleation mechanisms of vertically aligned ZnO-NR arrays and the effect of seed layers on density. The main disadvantage of this technique is that it is quite difficult to monitor the growth of nanostructures.

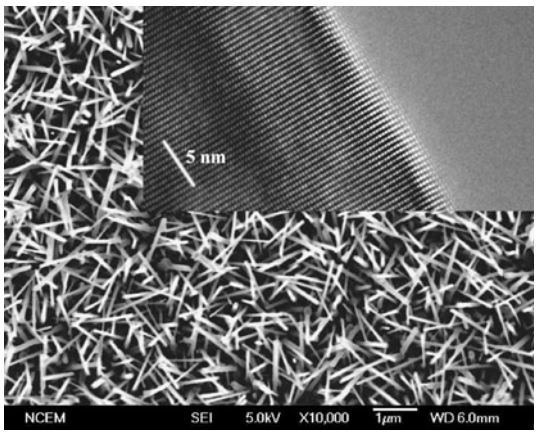

Fig. 11 Typical SEM image of femtosecond PLD grown ZnO-NWs. The *inset* shows the TEM image of a part side NW [118]

Optical properties of various 1D nanostructures

Optical properties in ZnO nanostructures as well as its refractive index were extensively investigated many decades ago. In this section, a review on the optical properties of 1D-ZnO nanostructure is given. The UV emission and origins of deep-level emission (DLE) band in ZnO photoluminescence (PL) spectra are briefly discussed.

PL properties

Room-temperature photoluminescence (RTPL) studies of the ZnO nanostructures focus on the proportion of UV-to-visible emission or the origin of defect emission. In addition to UV emission from RTPL spectra, there were one or more defect emission bands observed in the visible region [131]. Quantum confinement effects can also be observed from RTPL spectra for very small nanostructures (NRs with radius 1.1 nm) due to small size of exciton Bohr radius of ZnO (2.34 nm) [97, 132, 133]. Exciton binding energy is considerably improved due to 1D confinement. In addition, it was proposed that the green luminescence in ZnO involves free holes. But, bigger dimension ZnO (more than 1.1 nm) nanostructures are necessary for optical applications [133].

However, due to discrepancies in relative contributions of free exciton emission and phonon replicas, position of near-band-edge emission at room temperature could differ considerably, which was varied with growth conditions [133, 134]. We demonstrated the effect of oxygen plasma treatment on RTPL properties of ZnO-NRs and nanopagodas grown by chemical method, as described in "Chemical growth" section. Nanotip emitter had higher UV emission peak intensity than the nanopagodas and NRs, with minimum green emission peak intensity [78]. Intensity of visible emission decreases after oxygen plasma

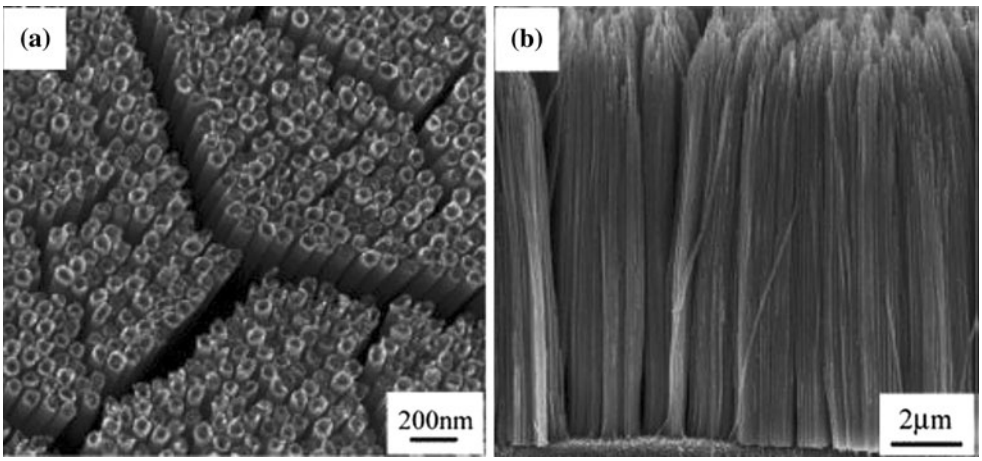

Fig. 12 SEM images of ZnO nanotube arrays grown by direct electrochemical deposition using anodic alumina templates **a** top and **b** cross-sectional view [124]

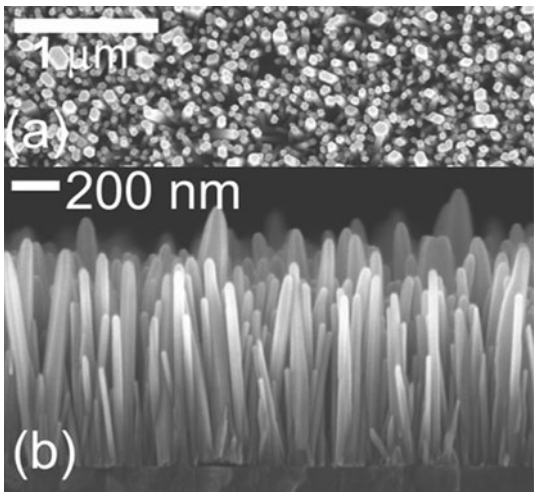

Fig. 13 Typical SEM image of the hydrothermally grown ZnO-NRs: **a** top and **b** cross-sectional view [128]

treatment and nanotip emitter had the lowest green emission intensity, due to decrease of oxygen vacancy. By implanting oxygen ion into ZnO-NRs through oxygen plasma treatment, oxygen vacancies of ZnO-NRs were decreased so it provided better UV emission than the as-grown NRs [78].

To understand the detailed information about defect states and impurity of ZnO 1D nanostructures, LTPL studies are mostly used. It was very difficult to find out defect emission from the RTPL study, although considerable amounts of defect density were present, which only exhibited prominent UV emission [128, 135]. The presence of free excitonic emission from LTPL spectra was used to find out the good optical quality of ZnO-NRs [136]. On the other hand, sample quality could be identified from the biexcitons binding energy (17 meV), which was occasionally noticed in the LTPL spectra of ZnO nanostructures [137]. Biexciton emission in MOCVD grown ZnO-NRs on sapphire up to 200 K was reported by Zhang et al. [138]. By using high-resolution measurements and precise determination of bound exciton peak positions of LTPL spectra, yield information about impurities of the nanomaterials could be observed. Bound exciton position peaks in details were reported in another review [133].

The emission peak of LTPL spectra at 3.342 eV in ZnO-NWs was allocated to excitons bound to structural defects at the surface of the NWs [139]. By using temperature-dependent and time-resolved PL spectra, defects and radiative decay in the ZnO nanostructures can be obtained. Constant PL intensity above 120 K and PL decay time of 800 ps at RT were observed in the MOVPE grown ZnO-NRs on GaN [140]. Subannajui et al. [141] reported the RTPL properties of polar c- and non-polar a-orientated ZnO-NWs by ionic liquid-assisted technique using GaN(0001) on sapphire substrate. RTPL spectra exhibited a big reduction of the green luminescence which involved an annihilation of DLE, and the possible mechanisms responsible for the green emission reduction were proposed.

Figure 14a shows the comparison of a typical RTPL spectrum of ZnO-NRs grown by VLS method with the bulk one [107]. At 3.311 eV, UV emission of ZnO-NRs is attributed to the excitonic one, originating from the recombination of free excitons [107, 142], while the origin of blue–green emission relates to oxygen vacancy (V_O). Typical temperature-dependent PL spectra of VLS grown ZnO-NRs are shown in Fig. 14b. Leading peak at 3.402 eV at above 50 K is attributed to free excitons. The peak is faintly blue shifted in contrast to the reported value (3.377 eV) for high-purity bulk ZnO [107, 143, 144]. As temperature increased, the near-band-edge emission peak shifts toward the lower energy side, due to the thermal

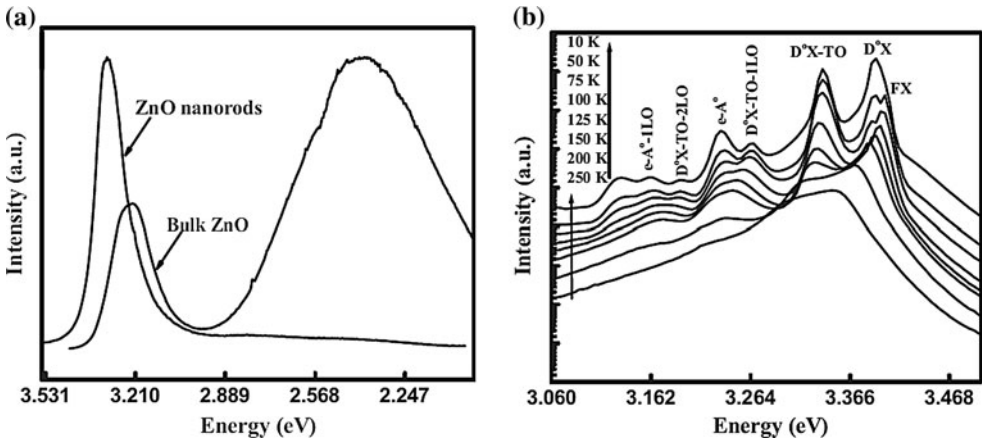

Fig. 14 **a** Comparison of the room-temperature PL spectra of VLS grown ZnO-NRs and bulk ZnO and **b** temperature-dependent PL spectra of VLS grown ZnO-NRs in the range of 10–250 K [107]

activation of carriers [145]. Free excitons peak at below 50 K is invisible; because the shallow donor-bound excitons can flow back and forth between two exciton states at extremely low temperatures [107, 146, 147]. Two-electron satellite transitions were observed in the NRs from LTPL spectra in energy range from 3.30 to 3.34 eV.

Time-resolved photoluminescence

Time-resolved photoluminescence (TRPL) studies were carried out for the various ZnO nanostructures, both for stimulated and spontaneous emission. Typically ultrafast spectroscopy studies revealed very fast decay for the stimulated emission [148–150]. Diameter dependence bi-exponential decay with decay time was observed in TRPL of CBD grown ZnO-NRs, and the variations in decay times were attributed to surface recombination [151]. Lettieri et al. [152] proposed a model which offered information of deep defect concentration ($\sim 10^{18}$ cm^{-3} for ZnO-NWs), bimolecular recombination, and unimolecular recombination. Richters et al. [153] studied PL properties of vapor-phase epitaxy grown ZnO-NWs, and they reported the features for identifying the surface exciton emission. Surface exciton recombination could be enhanced by coating the NWs with polymer dielectric.

Kwok et al. [154] obtained short spontaneous emission lifetimes in hydrothermally grown NRs and VLS deposited hollow spheres, but stimulated emission was observed only in NRs. Compared to single crystals and high-quality thin films, generally ZnO nanostructures revealed shorter PL lifetimes and higher nonradiative defect density. VLS grown aligned ZnO-NR arrays showed spontaneous emission of about 80 and 360 ps decay time and short decay time (under 30 ps) for stimulated emission [155]. Decay time increased with the increase of MOCVD grown ZnO-NRs size, attributed to the decrease in exciton–polaritons radiative rate [156].

MOVPE grown ZnO-NWs exhibited single exponential decay having time constant of 270 ps at RT, and decay time first decreased and then increased with increasing temperature for low nonradiative defect density nanostructures [157]. Oxygen partial pressure during growth had considerable effect on both the morphology and PL lifetime in PLD grown ZnO-NWs using femtosecond laser, and enhanced results was achieved at a lower pressure [118]. From the room-temperature TRPL study, the presence of thiourea in ZnO-NRs grown by pneumatic spray pyrolysis technique resulted in increasing the exciton lifetime [158].

Electrical properties

Importance of ZnO nanostructures is increased for its good transport properties. They are often configured in field effect transistor (FET) with a back gate for current transport studies and in field emitter devices. In this section, we review the electrical properties of ZnO 1D nanostructures.

Transport properties

Basic study of the electrical properties of 1D-ZnO nanostructures is essential for developing their potential applications in nanoelectronic devices. Several groups reported about the electrical transport properties of individual ZnO-NRs and NWs [159–165]. Using single ZnO-NW on SiO_2/Si(001) substrate, Chik et al. [160] fabricated field-effect transistor (FET). Fabricated NW FET structure with measurement circuit is schematically shown in Fig. 15a. In general, undoped ZnO-NW typically shows n-type conductivity, due to the native defects such as oxygen vacancies and zinc interstitials. It was anticipated that point defects in ZnO are projected to be copious owing to their low formation energies [166].

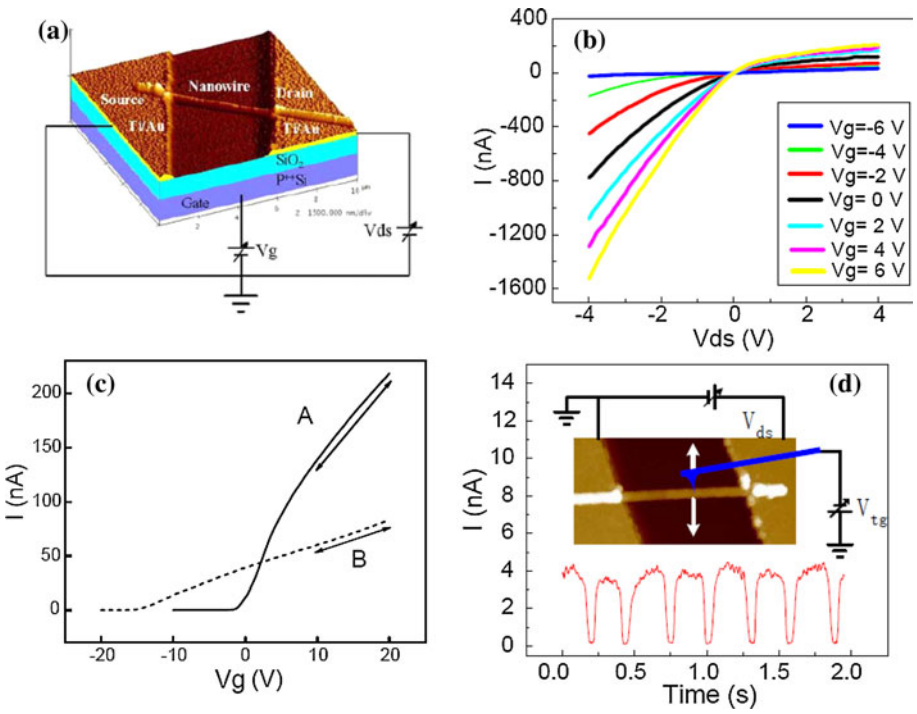

Fig. 15 **a** AFM image of a ZnO-NW FET with schematic of *I–V* measurement. **b** *I–V* curves of a ZnO-NW FET from $V_g = -6$ V to 6 V; **c** Change of the transfer characteristics of two NWs grown in different synthesis conditions. NW A has a mobility of 80 cm^2/V s and carrier concentration $\sim 10^6$ cm^{-1}; and NW B has a mobility of 22 cm^2/V s and carrier concentration $\sim 10^7$ cm^{-1}. **d** A demonstration of periodic modulation of the NW conductance by a scanning probe (*Inset* shows the schematic of measurement set up) [160]

I–V characteristics of the ZnO-NW FET under different back gate voltages are shown in Fig. 15b. Well-distinct transfer characteristics are shown in Fig. 15c [160]. Moreover, using conductive AFM (CAFM), the electrical properties of ZnO-NW FETs were reported [167, 168]. Furthermore, a scanning tip was capable to switch on and off the conductance periodically (Fig. 15d), demonstrating the prospective nano-electro-mechanical system application [160]. Superior electrical property was observed in the ZnO nanostructures than the polycrystalline film. Single-crystalline ZnO-NWs showed high electron field effect mobility (80 cm^2/V s) [159], than the mobility of ZnO TFT (7 cm^2/V s) [169]. However, Park et al. [165] demonstrated that high electron mobility of 1000 cm^2/V s could be achieved by coating the NWs with polyimide, by reducing the electron scattering and trapping at surface.

Main complexity of ZnO for wide-ranging electronics and photonics applications is the difficulty of p-type doping. Numerous p-type doping efforts have been reported, such as Ga and N co-doping, to obtained low resistive (0.5 Ω cm) p-type ZnO thin film [170–172]. The p–n homojunction diodes and LED can be fabricated from the p-type and n-type ZnO-NWs. In later section we will discuss about the LED devices based on ZnO 1D nanostructure. Complementary logic circuits can constitute FET, fabricated from the p-type and n-type NWs. Liu et al. [161] fabricated intramolecular p–n junction on ZnO-NWs by using AAM template.

Hydrothermally grown NRs held considerable concentration of hydrogen impurities, which is affected by conductivity [173]. Conductivity of ZnO-NWs could be notably altered by plasma exposure, decreased in oxygen plasma and increased in hydrogen plasma [174]. Temperature-dependent resistivity measurements of VLS grown ZnO-NRs with Au catalyst showed that the charge transport was a combination of thermally activated conduction and the nearest neighbor hopping, while NWs with high conductivity (metallic-like) showed surface-related conduction [175]. The hydrogen exposure shows metallic *I–V* characteristic, whereas nonlinear *I–V* characteristic was recovered with oxygen exposure [176]. Exposure to oxygen causes adsorption of oxygen ions, caused upward band bending, whereas exposure to hydrogen caused adsorption of hydrogen ions and formed O–H bonds with ZnO, and which resulted in downward band bending and occurrence of highly conductive layer in the vicinity of surface [176].

Schottky diodes were fabricated using CBD grown ZnO-NRs with high ideality factor and low rectification factor [177]. To improve the contact between ZnO and metals, the oxide surface was treated with H_2O_2. By treating with H_2O_2, the rectification factor as high as 10^6 and ideality factor of 2.4 were reported for Ag contact [177]. In addition, there are further considerations in characterizing methods of single NWs. Four- and two-probe methods may provide different results in characterization of single ZnO-NWs. Using four-probe method, higher conductivity was achieved [178]. Using scanning tunneling microscopy *I–V* characteristics of individual ZnO-NW/$La_{0.65}Sr_{0.35}MnO_3$ heterojunctions were measured and large rectification ratios (~ 40) were obtained [179]. Single ZnO-NW

junction with p-Si(001) was also characterized using CAFM in ultra-high vacuum [180].

Field emission properties

Inspite of electrical transport studies, field emission from the vertically aligned NWs or NRs has also been extensively considered [181–193]. Sharp-tip quasi-one-dimensional (Q1D) nanomaterial is an innate candidate for electron field emitter. Several groups have studied the field emission from vertically aligned ZnO nanoneedles and NW [181–189]. Tseng et al. [183] reported about the field emission properties of needle-like VLS grown ZnO-NWs on Ga-doped ZnO (GZO) film. Turn-on field was found to be $\sim$18 V/μm at a current density of 0.01 μA/cm^2 and the emission current could reach 0.1 mA/cm^2 at 24 V/μm, as shown in Fig. 16. Lee et al. [193] reported better emission current of 1 mA/cm^2 at 11 V/μm and turn-on field of 6 V/μm at 0.1 μA/cm^2 current density, which could afford adequate brightness as flat panel display.

We reported the field emission properties of the as-deposited chemically grown ZnO-NRs, nanopagodas and nanotips (Fig. 17) [78]. Growth process of the nanostructures is discussed in "Chemical growth" section. *I–V* emission characteristics analyzed by using Fowler–Nordheim (F–N) equation can be written as [190–193]

$$J = A\left(\frac{\beta^2 E^2}{\varphi}\right)\exp\left(-\frac{B\varphi^{1.5}}{\beta E}\right), \quad (1)$$

$$\ln\left(\frac{J}{E^2}\right) = \ln\left(\frac{A\beta^2}{\varphi}\right) - \frac{B\varphi^{1.5}}{\beta E}. \quad (2)$$

where J is the current density, E is the applied field, $A = 1.56 \times 10^{-10}$ (A eV/V^2), $B = 6.83 \times 10^9$ (V/eV$^{1.5}$ m), β is the field enhancement factor, and ψ is the emitter work function which is about 5.37 eV for ZnO. β approximately equals to $s \times d/r$, where s is dependent on screen effect, d is the anode to cathode distance, and r is the emitter radius [190].

Inset of Fig. 17a shows log(*I–V*) F–N plots of the NR field emitters indicating that turn-on electric fields of the as-grown, plasma etching, and two-step etching emitters are 6.01, 3.03, and 1.70 V/μm, respectively, at 1 μA/cm^2 current density. Stability of turn-on field of the different NR emitters is shown in Fig. 17b. A stable turn-on field is observed after two-step etching compared to the as-grown NRs, as shown in Fig. 17b. Turn-on and threshold electric fields of ZnO nanopagoda emitters are 1.46 and 2.32 V/μm, respectively. Nanopagoda and nanotip emitters reveal smaller tip angle and lower emitter number density than the NR emitters. Better field emission property of the nanopagoda and nanotip emitters is observed, due to the minimized screening effect between neighboring emitters [78]. The turn-on, threshold fields and current densities of nanotip emitters reach more stable values in comparison with those of the nanopagoda emitters, due to hexagonal

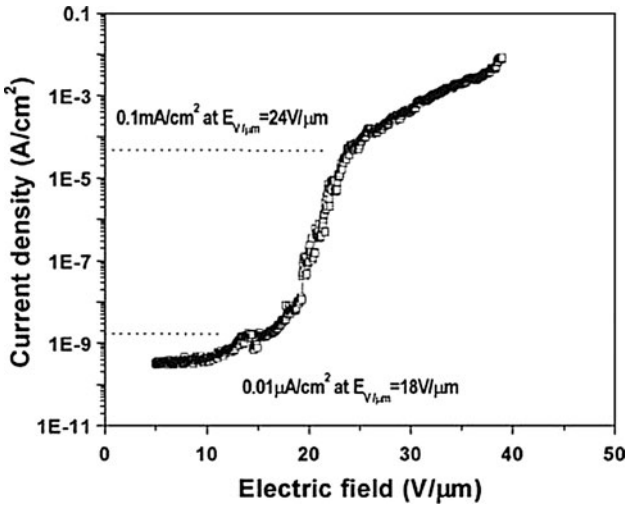

Fig. 16 Field emission *I–V* characteristics of VLS grown ZnO-NWs [183]

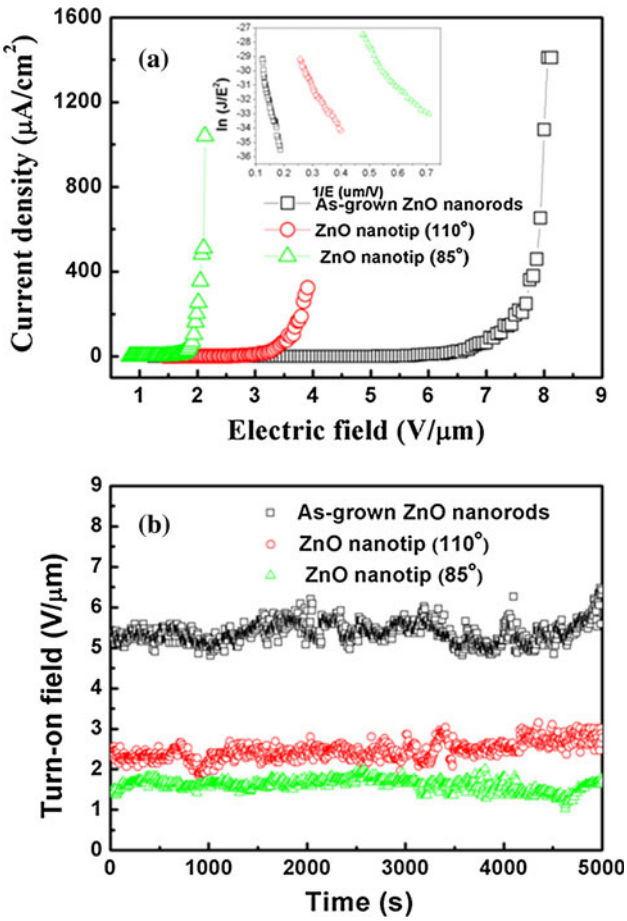

Fig. 17 **a** *J–E* curves (*inset* is F–N plots) and **b** stability test of the chemically grown ZnO-NR emitters [77]

edge area of ZnO nanopagoda emitters. We also reported [194] the field emission properties of a ZnO-NW triode which can be enhanced by illumination and argon ion bombardment.

Sensing properties of 1D nanostructures

Among solid-state chemical sensors, metal oxide semiconductor films are most promising for sensing applications. 1D-ZnO nanostructures have been used as active components in various sensors such as gas sensors [195–197], visible-blind UV sensors [198–200], visible light sensors [201], biosensors [16, 202, 203], and strain sensors [204].

Sensing properties depended on the resistance or piezoresistance change of NWs [205] or the change of barrier height at contact [204, 206–209]. Basic sensing method of metal oxide-based gas sensors relies on a variation in electrical resistivity due to interaction between the surface complexes such as O^-, O_2^-, H^+, and OH^- reactive chemical species and the gas molecules to be detected. This section reviews the different sensing properties of ZnO 1D nanostructures.

Gas sensor

Oxygen vacancies on metal oxide surfaces are electrically and chemically active. Oxygen molecules from the atmosphere are adsorbed onto the metal–oxide NWs surface and ionized to O_2^-, O^-, and O^{2-} ions by extracting electron from the conduction band of oxides [210–212]. O_2^- is chemisorbed at low temperature (commonly < 100 °C) while O^- and O^{2-} are chemisorbed at high temperature (commonly > 100 °C). These vacancies act as n-type donors and significantly increase the conductivity of oxide. Upon adsorption of charge-accepting molecules at the vacancy sites, such as NO_2 and O_2 (oxidation gas), electrons are effectively depleted from the conduction band, leading to a reduced conductivity of n-type oxide.

However, reduction gas would react with surface-adsorbed oxygen and consequently remove it, leading to an increase of conductivity. Most of the metal oxide gas sensors operate on this principle. ZnO bulk and thin films have been reported for NH_3, alcohol, and H_2 sensing under elevated temperature ($\sim$400 °C) [213–216]. From the aspect of sensing performance, 1D-ZnO nanostructure is expected to be superior to its thin film counterpart. Sensing properties of ZnO 1D nanostructures were obtained in the form of aligned nanotubes, NWs, and mesh of NWs. Bie et al. [217] prepared nanopillar ZnO (diameter 10–30 nm) array sensor by chemical method on Al_2O_3 directly. Almost linear response of the sensor to ethanol was reported in the range of 250–2500 ppm, whereas hydrogen response did not differ so much in the concentration range from 500 to 2500 ppm [217].

Hsueh et al. [218] reported ethanol sensors of evaporated ZnO-NWs on 50-nm-thick GZO as a patterned bottom contact. A selective number of NWs (80 nm diameter) grew laterally and linked two neighboring fingers to provide ohmic electrical paths. Quite small relative response of 0.6 was reported compared to other ZnO nanostructure-based sensors, by using high ethanol concentration. Good ethanol sensing properties of metal catalyst-free ZnO-NWs (diameter $\sim$25 nm) grown by thermal evaporation was observed by Wan et al. [219]. Sensor response (S_G) was found to be 47 and 1.9 at 200 and 1 ppm ethanol exposure, respectively, at 300 °C. This could be explained as, if the diameter of the ZnO-NWs is comparable to Debye length (L_D), the space charge region occupies the entire wire due to the presence of adsorbed surface state and hence switching conductivity is observed.

Ethanol (100 ppm), H_2S (2 ppm), HCHO (50 ppm), LPG (500 ppm), 90 % gasoline (50 ppm), CO (500 ppm), and ammonia (50 ppm) gas sensors of hydrothermally grown ZnO-NR (diameter 40–80 nm) powders was reported by Xu et al. [220]. As shown in Fig. 18, ZnO sensors show relative high sensitivity to inflammable gases such as LPG, alcohol, and 90 % gasoline, so it can be used as sensitive sensor to detect inflammable gases. H_2, CH_4, NH_3, ethanol, and H_2S gas sensor using hydrothermally grown ZnO-NRs (diameter 70–110 nm) paste was also reported by Wang et al. [221]. It showed high response to ethanol when operated at 350 °C and a high response to H_2S at 25–200 °C in dry air carrier gas. H_2- and ozone-sensing properties of MBE grown ZnO-NRs (diameter 30–150 nm) were also reported [113]. Lupan et al. [222] reported the single ZnO-NW-based nanoscale sensor fabricated using focused ion beam (FIB/SEM) instrument. An interesting approach of vertically aligned ZnO-NWs

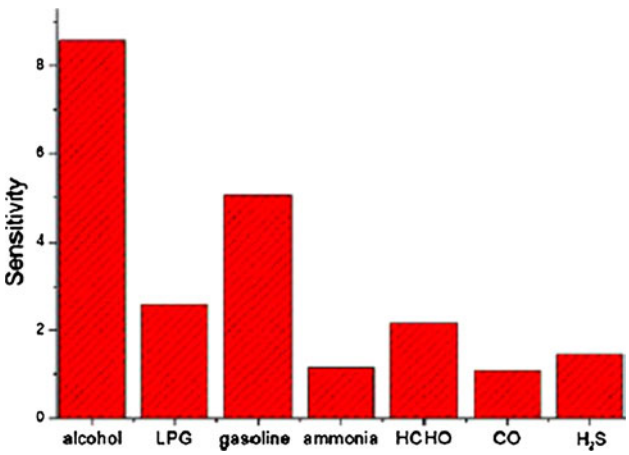

Fig. 18 Response of hydrothermally grown ZnO-NRs gas sensor to different gases at 330 °C working temperature [220]

devices for methanol and nitrous oxides sensors was demonstrated by Parthangal et al. [223].

Hydrogen detection properties of Pd-catalyzed MBE grown ZnO-NWs was studied by Wang et al. [114]. Tien et al. [224] compared the performances of H_2 detection between Pt-coated (thickness = 10 Å) single ZnO-NRs and thin films as a function of film thickness grown by PLD on sapphire substrates. At room temperature, Pt-coated NRs had a better response ($S_G = 1.08$ for 500 ppm H_2) than thin film approximately by a factor of 3. By comparing with the Pd-catalyzed samples, Pd-catalyzed ZnO-NWs seemed to exhibit much better H_2 detection compared to that catalyzed with Pt, giving higher response to a H_2 concentration 50 times lower [224]. NH_3, H_2, LPG, and C_2H_5OH gas sensing of ZnO-NRs (diameters ~10–30 nm and lengths ~150–250 nm) prepared by one-step solid-state reaction was studied by Sun et al. [225]. Different ZnO nanostructures such as NRs (diameter 30–40 nm), NWs (diameter 20–30 nm), and nanotubes (diameter 60–100 nm) were prepared by Rout et al. [226] to study the sensing properties. To prepared thick film sensor, diethyleneglycol was added along with the ZnO nanostructures to form a paste and a comb-type structure having Pt electrode in one side and heater on the other side was obtained. NWs revealed the best sensing properties toward hydrogen (down to 10 ppm of H_2) sensing at relatively low temperatures (150 °C) among the others.

Sensor based on single defective ZnO-NW having a big diameter (400 nm) was also demonstrated [227]. Schematic configuration (Inset of Fig. 19a) and SEM image of a single ZnO-NW gas sensor are shown in Fig. 19a. Higher H_2S sensitivity was observed for the implanted ZnO at 1×10^{16} cm^2 than unimplanted one, as shown in Fig. 19b, c. Due to the defects of modulation on electron concentration in NW, the gas response on implantation is varied. Trapped electrons are released from the ZnO once exposing it to H_2S, as a result electron concentrations are increased. The response difference was bigger for the unimplanted NW, since implanted NWs had much less conductance electron [227]. Shalish et al. [228] proposed that ZnO-NWs exhibited interesting gas-sensitive PL properties. Air- and NO_2- sensitive PL properties of ZnO-NWs were also demonstrated [229]. Study of different gas sensing properties, such as NO_2, ethanol, and relative humidity, by dynamic PL quenching of ZnO-NW were also reported [230].

Biosensor

Nanostructures of ZnO have drawn many attractions for biosensors application with several benefits, including biological compatibility, nontoxicity, easy preparation, and fast electron transfer rates [16, 17, 231–242]. ZnO-NRs could be used for uric acid biosensors [232]. Kong et al. [240] fabricated glucose biosensor by immobilization of glucose oxidase onto ZnO nanotubes via cross-linking method. Due to good biocompatibility and intrinsic porous structure of ZnO nanotubes, the fabricated glucose biosensor demonstrated extremely sensitive and fast response to glucose with fairly broad linear range from 50 μM to

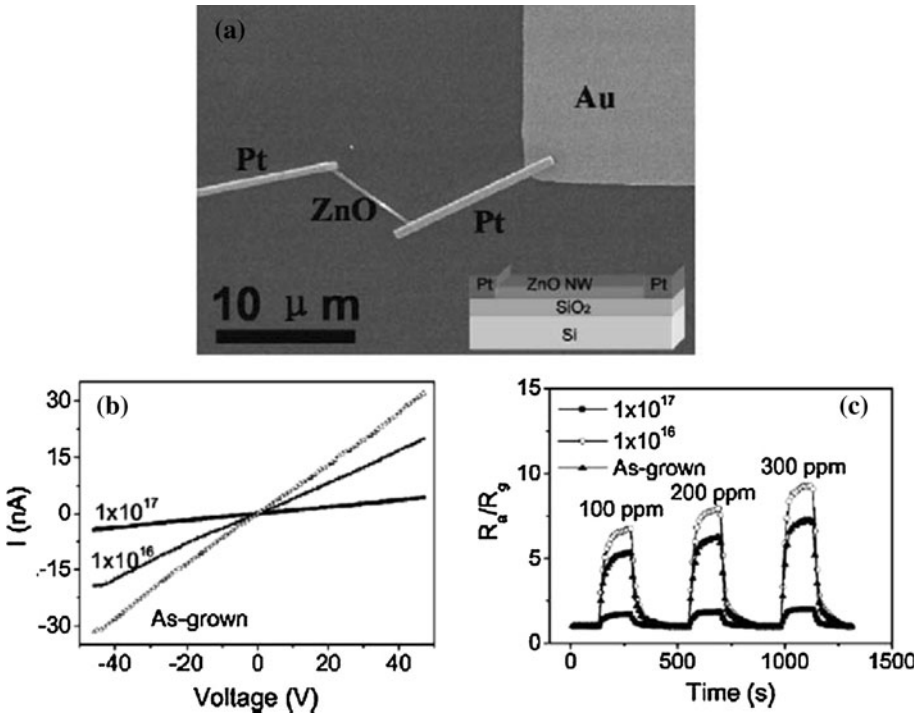

Fig. 19 **a** Schematic configuration and SEM image of a single ZnO-NW gas sensor. **b** *I–V* curves and **c** dynamic response curves for different H_2S concentrations of a single ZnO-NW gas sensor at different implanted doses [227]

12 mM and could sense as low as 1 μM glucose without any electron mediators.

A high-performance glucose sensor through immobilization of the glucose oxidase using ZnO-NW has been demonstrated by Zang et al. [236]. The high sensing performance was attributed to its high specific surface area and high isoelectric point value for capable immobilization of high concentration of acidic enzymes and the mediating effect by redox reaction of ZnO-NWs. It offered a general approach to tailor the oxidase enzyme-based biosensor for ample variety of applications.

Asif et al. [242] demonstrated intracellular glucose sensors for concentration in single human adipocytes and frog oocytes of the hexagonal ZnO-NRs (diameter of 100–120 nm and a length of 900–1000 nm) grown on submicron silver-covered capillary glass tips. Nanosensor based on ZnO-NRs was used to measure the free concentration of intracellular glucose in a single human adipocyte. The glucose-selective nanoelectrode, mounted on a micromanipulator, was moved into the location in the same plane as the cells and placed in a short distance by micromanipulating. Due to the excellent electrostatic interaction with ZnO-NRs and glucose oxidase, glucose oxidase retained its enzymatic activity. The intracellular biosensor showed a fast sensing response (time constant < 1 s). Sensing effect of the intracellular glucose concentration after application of insulin hormone was also reported. The proposed ZnO-NR-based biosensor can be applicable in medical, food, or other areas of the mankind.

PH sensor

Normally ZnO shows amphoteric nature, with 9.5 IEP [236]. An intracellular pH sensor by using ZnO-NWs as an electrochemical probe was reported by Al-Hilli et al. [243]. Due to the change of surface potential in NW, the surrounding pH was changed, which was noticed as a voltage variation between the working and reference electrodes. Within pH range of 4–11, electrochemical potential was almost linearly proportional to the pH of buffer electrolyte, with a sensitivity of $\sim$52 mV/pH. The intracellular pH value of 6.81 was also reported by using human fat cell. Due to the nontoxic and biocompatible properties of ZnO [236, 244–247], the intracellular measurement did not visibly influence the cellular viability so this procedure could be an effective way of in situ pH measurement in single living cell.

Electronic device applications of 1D nanostructures

Tremendous attraction in ZnO is stimulated and fanned by its prospects in optoelectronics device applications. As a consequence, ZnO is recognized as a promising photonic material in the blue–UV region. In this section, we review the applications of the 1D-ZnO nanostructures in different electronic devices.

Homo- and heterojunctions LED applications

A variety of light-emitting devices based on 1D-ZnO nanostructures have been reported to date. Increase of light extraction efficiency up to 57 % using ZnO-NRs in GaN-based LEDs was proposed [248].

Homojunction LEDs

Vapor-deposited As ion-implanted ZnO-NR array-based ZnO homojunction LED on n-Si(001) was reported [249]. Ion fluence-dependent EL spectra exhibited red emission in 10^{15} ion fluence whereas it exhibited UV emission with weak red peak in 10^{14} ion fluence. Amplified spontaneous emission was reported in the latter case [249]. Ambipolar charge transport was observed in hydrothermally grown ZnO-NRs, with electron and hole mobilities of 3.2 and 2.1 cm^2/V s, respectively. The devices showed yellow electroluminescence and dominant broad yellow–orange defect emission [250]. Arsenic-diffused ZnO homojunction NW LED devices on GaAs were fabricated by annealing [251].

Heterojunction LEDs

It was proposed that compared to thin film-based devices, NW-based devices had higher efficiency, due to possibility to attain increased light extraction [252]. Efficiency was expected to improve due to the improved injection through a nano-sized junction [253]. ZnO heterojunctions LEDs based on a combination of ZnO with a variety of materials including silicon substrate and organic materials have been briefly reviewed by Djurišić et al. [133]. Uses of p-Si(001) substrate or organic materials represent a simple and straightforward choice for LED device fabrication. UV and green emissions were observed in the p-Si(001)/n-ZnO-NR device [254, 255].

LEDs based on n-ZnO-NRs/p-$CuAlO_2$/p-Si(001) and n-ZnO-NRs/p-Si(001) grown by vapor deposition method have also been demonstrated [256]. Diodes showed very good rectifying properties with highly asymmetric *I–V* curves [256]. Improved rectification properties with visible electroluminescence have been observed in the MOCVD grown p-Si(001)/ZnO-NRs/ZnO film [257]. Single n-ZnO-NW/p-Si(001) heterojunction device, using NWs with different growth directions, showed UV emission (and some broad emission band at $\sim$700 nm) at forward bias [258]. Different

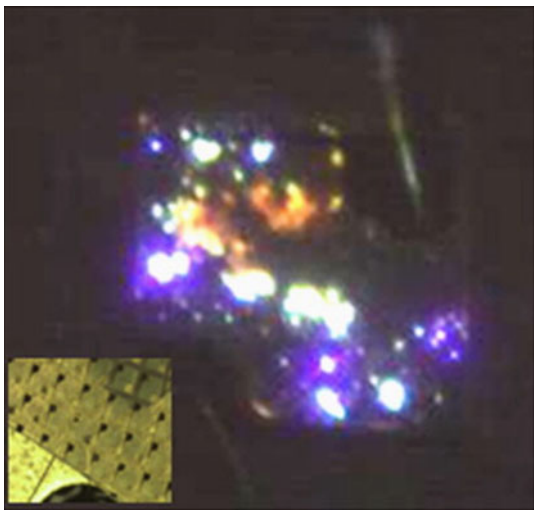

Fig. 20 EL emission micrograph of hydrothermally grown ZnO-NR/p-GaN heterojunction LED chip emitting *violet*, *yellow*, and *white* light at an injection current of 10 mA under forward bias. *Inset* shows the optical microscope image of ZnO-NR/p-GaN heterojunction LED arrays with an individual 300 × 300 μm^2 chip [271] (Color figure online)

heterojunction LEDs based on 1D-ZnO nanostructures with different polymers have been reported [259–270].

For the fabrication of ZnO heterojunctions, GaN remains one of the most common ones, due to relatively small lattice mismatch between GaN and ZnO. A variety of emission colors were observed in the GaN/ZnO-based LEDs by varying the properties of ZnO and GaN, as well as by varying the device architecture [133]. Impact of the hydrothermally grown ZnO-NRs density on light emission was investigated [269]. LEDs based on these NRs were also demonstrated, with the space between the NRs filled by a SiO_2 passivating layer [271]. Light emission under forward bias was detected, but the emission was rather non-uniform, as shown in Fig. 20. At 40 mA (80 V bias), violet emission centered at 415 nm and broad emission band from 485 to 750 nm were observed from the emission spectra. Violet emission was attributed to the thermal shift due to large injection current into ZnO-NRs [271].

Intense light emission under both forward and reverse biases was observed from the ZnO-NRs-based LEDs fabricated by low-temperature hydrothermal method on unetched GaN LED wafers [272]. Hydrothermally grown ZnO-NRs on p-GaN devices exhibited a combination of violet and blue emissions under forward bias with good rectifying properties [252]. MOCVD grown ZnO-NRs and ZnO film-covered NRs having structure p-GaN/n-ZnO-NR/n-ZnO on sapphire with and without GaN film exhibited rectifying *I–V* curve and blue light emission under forward bias [273]. Devices with undoped ZnO-NRs sandwiched between p-GaN and MOCVD grown Al-doped ZnO film were also reported [253]. Pure UV electroluminescence from ZnO-NR/p-GaN LEDs prepared by solution method was demonstrated at low bias-voltages (~4.3 V) [274]. However, UV–violet emission has been observed in the devices with NWs between p-GaN and undoped ZnO film, which became more intense after hydrogen treatment [275]. All the devices showed rectifying characteristics and UV–violet light emission, but performance of the NW devices was improved compared to thin film devices [276].

Despite the fact that most of the ZnO-NR/p-GaN devices revealed light emission under forward bias, a device which lighted up under reverse bias was also demonstrated [52, 272, 277]. An [277] demonstrated reverse tunnel junction of GaN LEDs using transparent vertical-aligned ZnO-NR arrays for nanoelectrodes. Such devices exhibited three times enhanced light output power compared with that of GaN LEDs with tunnel junction ZnO thin film due to the increased light extraction efficiency [277]. LEDs based on n-GaN/ZnO coaxial nanostructures on p-GaN substrates showed UV and blue emission [278]. Strong green and blue emissions were observed in the devices of GaN/InGaN-MQW/p-GaN (MQW: multiquantum well) deposited coaxially over the MOVPE grown ZnO nanotube templates (diameter 500 ± 50 nm and length 6.0 ± 0.2 μm) [279]. Hydrothermally grown ZnO-NRs on commercial LED wafer (GaN/InGaN-MQW/p-GaN) substrate have also been demonstrated [280]. Not only that n-type ZnO-NWs or NRs have been used for LED applications, LED based on p-Type ZnO-NWs and NRs on n-Si and n-GaN have also been reported [281, 282].

Amin et al. [283] scaled up (5 g in each batch) the ZnO-NRs synthesis by hydrothermal method and they used it for heterojunction LED application. Further, a printable composition was proposed by mixing ZnO-NRs into a common solvent-based screen-printable varnish on the flexible polymer substrate and flexible LED was fabricated. Same group [284] also reported the intrinsic white light emission of an ZnO-NRs-organic poly(9,9-dioctylfluorene) hybrid LED grown at 50 °C on a paper substrate. The hybrid LED indicated clear rectifying behavior and a broad band electroluminescence peak covering the whole visible spectrum region.

Photodetector

ZnO gives a lot of interest for application in photodetectors, in particular visible–blind UV detectors, as a wide band gap semiconductor. UV-light irradiation of the nanoparticles device of ZnO in air was observed to result in a significant increase of the conductivity [285]. These processes could be observed by introducing ON/OFF switch between light source and the ZnO nanostructure as listed in the following:

Initial state

$$O_2(g) + e^- \rightarrow O_2^-(ad), \quad (3)$$

Switch ON

$$h\nu \rightarrow e^- + h^+, \quad (4)$$

$$h^+ + O_2^-(ad) \rightarrow O_2(g), \quad (5)$$

Switch OFF

$$O_2(g) + e^- \rightarrow O_2^-(ad). \quad (6)$$

Upon illumination, photogenerated holes discharge surface-chemisorbed O^{2-} through surface electron–hole recombination, while the photogenerated electrons significantly increase the conductivity. When illumination is switched off, O^{2-} molecules re-adsorb onto nanostructure surface and reduce the conductivity. In general, the properties of the photodetector were demonstrated to be improved through nanostructure.

Chemically grown ZnO-NRs UV photodetector was reported by us [286]. The ZnO-coated substrates are immersed in a precursor solution for 60, 30, 20, and 10 min (ZnO-*x*, x = growth time), respectively. Figure 21a shows *I–V* characteristics of the ZnO-10 (growth time for 10 min) NRs photodetector measured in dark and under UV illuminations. Small dark current of 63.2 nA at 0.5 V DC bias is observed from the photocurrent measurement. The low dark current is caused by the formation of depletion layer near surface by adsorbed oxygen molecules in dark environment [$O_2(g) + e^- \rightarrow O_2^-(ad)$]. When the ZnO-NRs are exposed under UV, they generate electron–hole pair [$h\nu \rightarrow e^- + h^+$]. Trapped electrons are released back to the conduction band when the photo-generated holes reacted with the adsorbed oxygen molecules [$h^+ + O_2^-(ad) \rightarrow O_2(g)$] [286–290].

Figure 21b shows the time-resolved photocurrent of the ZnO-10 NRs photodetector in response to turn-on and turn-off of the UV illumination with different power densities. The photocurrent exponentially increases from 29.2 nA to 1.55 μA within about 100 s and then gradually saturates in turn-on state with a power density of 70 μW/cm^2. After the UV light was turned off, the current decreases to 63.2 nA within 120 s [286]. The sensitivity versus time curves under 100 s illumination of the photodetectors are shown in Fig. 21c, revealing that the times of the current recovering to initial value of the ZnO-10, ZnO-20, ZnO-30, and ZnO-60 photodetector are 120, 210, 290, and 470 s, respectively. The ZnO-10 photodetector has faster recovery rate in comparison with other photodetectors. Because, ZnO-10 NRs have relatively shorter electron transmission length compared to other larger radius NRs [285, 291].

Figure 21d shows the sensitivity of less than 100 s illumination of the ZnO-NRs-based photodetector as a function of growth time, indicating that the sensitivity of ZnO-based photodetector increases with an increase of UV light power density and a decrease of growth time. However, under longer time illumination (over 150 s), the longer NR (ZnO-60) photodetector exhibits higher sensitivity under 25 μW/cm^2 UV density (Fig. 21e) because ZnO-60 provides larger surface area [286]. To further evaluate the photodetector performance of the ZnO-10/PET structure, the orientation, retention, stability, and multi-UV intensity characteristics were measured and demonstrated [286]. Table 1 summarizes and compares the performance of various ZnO 1D nanostructures-based photodetectors [198, 292–298]. It indicates that ZnO-10/PET photodetector has faster response and recovery rate under various UV intensity illuminations, higher reliability, excellent orientation properties, and multi-level photoresponse in comparison with other reported photodetectors [286].

The p-Si/n-ZnO-NW heterojunctions-based photodetectors exhibited rectifying behavior [299]. Responsivity of ZnO photodetectors based on ZnO-NWs on ZnO:Ga/glass substrates to UV light (362 nm) was 0.03 A/W at a bias of 15 V [300]. Rise and decay constants of UV photoresponse of ZnO-NW-based photodetectors on ITO were 45 and 55 s, respectively [295]. UV photodetector based on laterally interconnected ZnO-NRs grown by CVT method on porous silicon substrates were demonstrated by Rajabi et al. [301]. Fast response photodetectors (0.1 ms rise time, biexponential decay with 0.09 and 0.36 ms time constants) were prepared by vapor-deposited ZnO-NWs [302]. Photodetectors based on ZnO nanoflake and NW prepared by localized oxidation of Zn exhibited relatively short time constants of 20.35 and 3.9 ms for rise and decay times, respectively [303]. Single ZnO-NW Schottky photodiode with Pt contact has been demonstrated [304].

Fan et al. [305] reported ZnO-NWs-based devices using without annealed AAM revealed positive photoconductivity, while devices fabricated in annealed AAO showed negative photoconductivity. No significant influence on the photodetector performance with ZnO-NW diameter up to 370 nm of UV region was investigated by Ha et al. [306]. Also, a ZnO-NW FET functioning as a UV photodetector was also demonstrated [307]. Annealing effect of hydrothermally grown n-ZnO-NRs/n-Si photodetectors was reported [308]. ZnO-NWs array on Si showed UV detector under reverse bias and visible detector under forward bias with good rectification ratios [309]. Hasan et al. [310] proposed UV sensor based on ZnO nanocrystals, made on common pencil drawn circuit over a paper.

Laser diode

ZnO was suitable for blue optoelectronic applications with UV lasing action for its wide band gap [311–313]. For wide band gap semiconductor materials, a high carrier

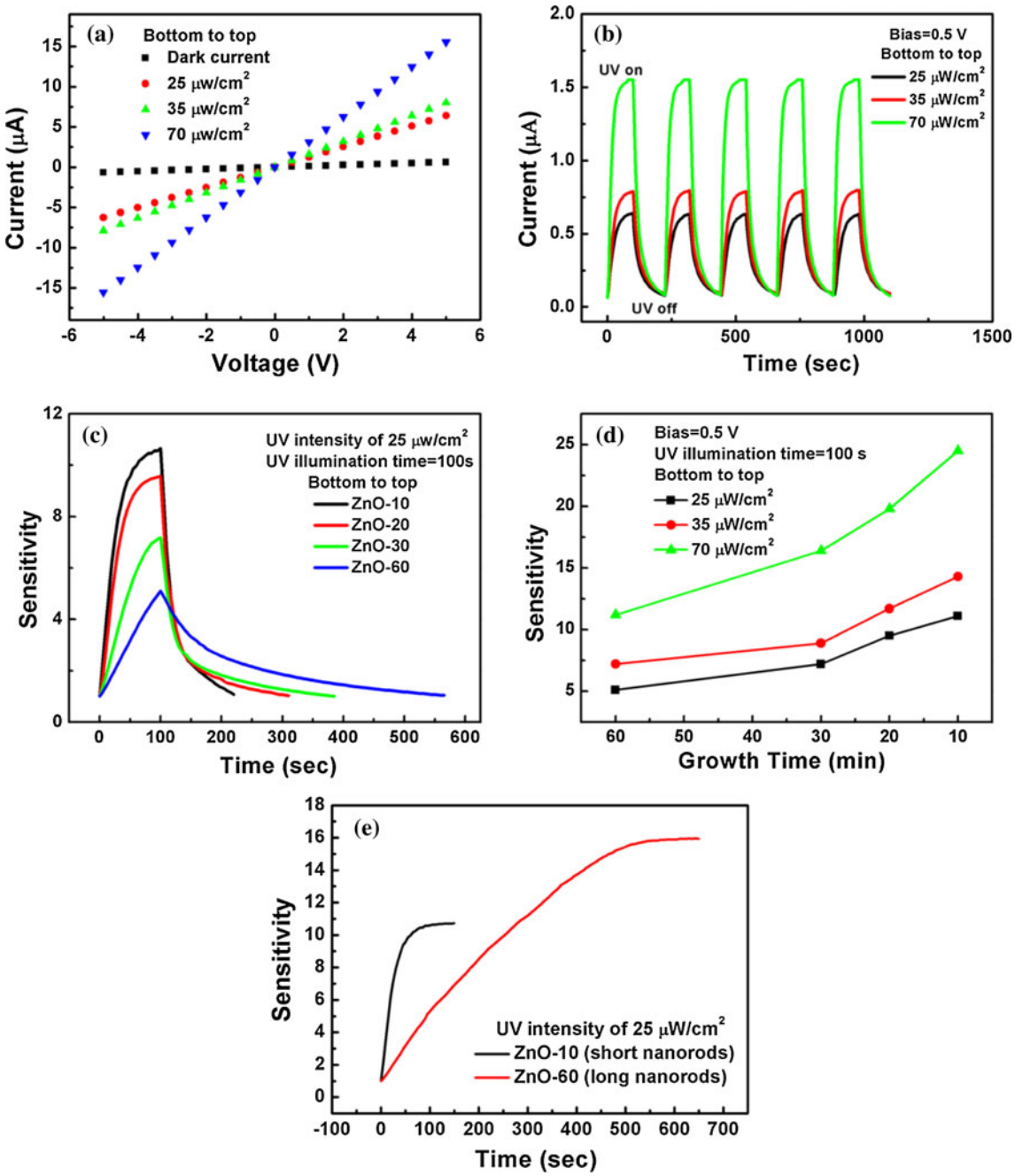

Fig. 21 **a** *I–V* plot of ZnO-10 NRs in dark and under UV illumination (365 nm) with various power densities. **b** Reversible switching properties of ZnO-10 NRs. **c** Sensitivity versus time plots under 100 s illuminations of ZnO-NRs grown with various times at 25 μW/cm^2 power density. **d** Sensitivity versus growth time curves of the NRs at 0.5 V bias under 100 s illuminations. **e** Sensitivity versus time plots of longer (ZnO-60) and shorter (ZnO-10) NR photodetectors under longer time illumination [286]

concentration was generally requisite in order to achieve high optical gain for lasing action in an electron–hole plasma (EHP) process [314]. Efficient excitonic laser action at room temperature can be achieved, if the exciton binding energy is much greater than the thermal energy (26 meV). In this respect, ZnO is a superior contender for its high exciton binding energy (∼60 meV). Threshold for excitonic lasing action can be lowered using low-dimensional compound semiconductor nanostructures, in which quantum size effects yield a considerable density of states at the band edges and improve radiative recombination due to carrier confinement [3].

Room-temperature lasing action was reported in VLS grown ZnO-NWs during evolution of emission spectra. At low excitation intensity, the spectrum consists of a single wide spontaneous emission peak and the spontaneous

Table 1 Comparison of photodetector properties for various ZnO nanostructures-based photo detectors

Type of ZnO nanostructures	Substrate	UV intensity ($\mu W/cm^2$)	Response time (s)	Recovery time (s)	Reliability	Reference
Nanoparticles (in O_2)	Silicon	20	≈10	≈50	4 cycles	[292]
Nanotubes	Glass	–	≈130	≈250	4 cycles	[293]
Single microtube (in O_2)	–	21700 at 50 cm distance	≈15	≈1850	4 cycles	[294]
Nanowires	Glass	1000	40	55	–	[295]
Nanorods	Paper	–	≈800	≈600	5 cycles	[301]
Nanorods	Glass	300	≈300	≈500	4 cycles	[297]
Nanorods	Silicon	16	≈100	≈150	12 cycles	[298]
Nanorods	PET	25, 35, 70	100	120	20 cycles retention (1, 50, and 100 h)	[286]

emission was at 140 meV below the band gap. Sharp peak with <0.3 nm linewidths appeared in the emission spectra as excitation intensity exceeds the threshold (~40 kW/cm^2). Integrated emission intensity rapidly increased above the threshold with pump power. The reported single or multiple sharp peaks signified different lasing modes at 370 and 400 nm wavelengths and areal density of these nanolasers was 1.1×10^{10} cm^{-2} [3]. External differential quantum efficiency (EDQE) of nanolaser based on ZnO-NW grown by PLD was reported by Zhang et al. [118]. It was reported that EDQE and internal quantum efficiency of ZnO-NWs (length = 7.5-μm)-based laser were 60 and 85 %, respectively [118]. The absolute light emission intensity of 0.1 mW was reported for individual NWs. Detailed analysis of the lasing properties of ZnO-NWs was also studied by Johnson et al. [315]. Pump power dependence laser emission revealed numerous tendencies which were clarified using dispersion and the exciton to EHP transition as a model [315].

RS of ZnO 1D nanostructures

Significant progress has been described in the applications of various 1D-ZnO nanostructures-based electronic, optoelectronic, and sensor devices. The Next-generation nonvolatile memory (NVM) has attracted growing interest as conventional charge-storage-based flash memories move toward their scaling limits [316–320]. To overcome this issue, several emerging NVMs, including ferroelectric random access memory, phase-change random access memory, magnetic random access memory, and resistance random access memory (RRAM) have been proposed, as a substitute for flash memory [320–332].

Among several emerging memory technologies, RRAM is one of the promising candidates because of its simple constituents, low operation power, high operation speed, and high integration density. Current–voltage characteristics of metal–insulator–metal (MIM) thin film capacitor structures exhibit a huge change in resistance between high resistance state (HRS) and low resistance state (LRS). RRAM devices has projected the advantages of nonvolatility, high density, fast switching speed, satisfactory switching endurance, and low power consumption [320–334]. As a result, it has been aggressively investigated to replace the present flash memory and extensively considered as the most potential candidate for the next-generation NVM application.

Generally RS is two types: unipolar and bipolar, depending on the relation between electrical polarity and RS phenomenon. For unipolar switching the switching procedure is dependent on the amplitude of applied voltage but independent of voltage polarity. In contrast, characteristic is called bipolar when turn-on process occurs at one voltage polarity and turn-off process at the reversed voltage polarity. In some cases both the switching (unipolar and bipolar) is observed called nonpolar switching. A number of binary metal oxide thin films, including ZrO_2 [328–330], HfO_2 [326], TiO_2 [323], NiO [324], and ZnO [331–336] has been proposed for RRAM applications because of their exceptional characteristics. Among these, ZnO-based film is one of the most promising materials for RRAM applications because of its high transparency, high reliability, and stable RS behavior [331–336]. Basic mechanism of RS operation is the formation and rupture of conducting filaments formed by oxygen vacancies or ions. Compared with thin film RS devices, a 1D nanostructure can provide a localized conducting filament in devices that allow RS operation with a narrow dispersion of operation parameters. In this section, we review the RS properties of all types of 1D-ZnO nanostructures.

RS in undoped nanostructures

Chang et al. [331] first proposed RS devices based on vertically aligned ZnO-NRs on ITO substrate grown by low-temperature chemical solution method. Sputtered Pt

was used as top electrode. Figure 22 shows typical *I–V* switching characteristics of Pt/ZnO-NR/ITO capacitor. It reveals an asymmetric *I–V* relation with memory hysteresis. When the applied voltage swept to a positive value above a specific voltage (0.7 V) called "set" voltage (V_{set}), the leakage current suddenly jumps from HRS to LRS (shown by arrow), the device is switched ON. By applying negative voltage sweep (−0.6 V), at particular voltage called "reset" voltage (V_{reset}) the device switches back to HRS again, the device is switched OFF. The Pt/ZnO-NR/ITO capacitor demonstrates reversible bipolar RS behavior. Compliance current (I_C) of 0.01 or 0.02 A was used to protect the samples from a permanent breakdown. Resistance value of LRS decreases and required reset current for switching LRS to HRS increases, with the increase of I_C (Fig. 22). This attributed to the formation of stronger filament which provides higher conductivity [332], or formation of more parallel filaments between top and bottom electrodes [333]. Distinct geometry of ZnO-NRs would give rise to the formation of straight and extensible conducting filaments along the direction of each single-crystalline ZnO-NR, directing to a stable RS behavior with a narrow dispersion in switching parameters.

Single ZnO-NW-based unipolar stable RS memory has been demonstrated first by Chiang et al. [334], as shown in Fig. 23. ZnO-NW was fabricated by evaporation and Ti was used as a top and bottom electrode. Creation of oxygen-depleted region at ZnO-NW surfaces and around the Ti/ZnO interface plays a crucial role in the RS behavior of single ZnO-NW RRAM. An initial forming process has been adopted by applying high voltage (∼22 V) for this single NW-based RRAM device. Inset of Fig. 23 shows the test MIM structure using two metal Ti contacts. Negative differential resistance (NDR) is clearly observed at ∼12 V. The "set" process occurs by decreasing the voltage to ∼7 V, the device returns back from HRS to LRS (resistance ratio = 7.7×10^5). By increasing the sweeping voltage, the endurance of switching cycles could be enhanced [334].

Yang et al. [335] demonstrated nonvolatile bipolar RS memory based on bottom-up single-crystalline ZnO-NWs and Cu and Pd as top and bottom electrodes, respectively. A 1–3 V bias sweeping has been performed for unsuccessful forming, prior to exhibiting successful bipolar switching process. Low threshold voltages of ≤3 and ∼−1.6 V were required for "set" and "reset" of the device, respectively. Cu/ZnO-NW/Pd memory device exhibited a large ON/OFF ratio of $>10^5$ and a long retention time of $>2 \times 10^6$ s. Switching in this device was induced by the formation/annihilation of metal filament at ZnO-NW surface indicated from the EDX elemental mapping [335]. Wu et al. [336] reported that the switching characteristics of PVD grown ZnO-NWs (500 nm and lengths of 50 μm) can be managed and modulated by piezotronic effect [19]. Inset of Fig. 24a shows the fundamental structure of the piezoelectrically modulated RS memory (PRRAM), which consists of a ZnO-piezotronic-NW (ZnO-PNW) connected with Au electrodes fabricated by lithography on a flexible PET substrate. Oxygen plasma treatment was performed in PRRAM cells to create tensile/compressive strain in the NWs by deforming the substrates before characterization, as shown in Fig. 24d.

As the applied bias increased from 0 to 10 V in the sample treated with 30-min oxygen plasma, the output current of PRRAM cell increased abruptly at 5.73 V, called threshold point $V_{th,S}$, and the device is switched from HRS to LRS, as shown in Fig. 24a. As the voltage was consequently reduced toward negative values, PRRAM cell switched back to high-resistance OFF state. However, when the bias exceeded certain negative values ($V_{th,D} = 5$ V in Fig. 24a), the PRRAM cell was switched to ON state again and there was a successive decrease in the value of negative

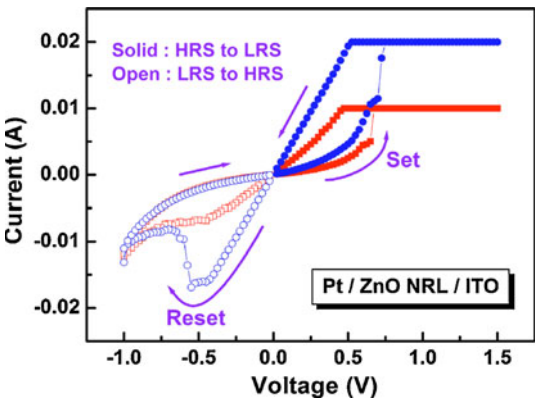

Fig. 22 Bipolar RS behavior of Pt/ZnO-NR/ITO capacitor [331]

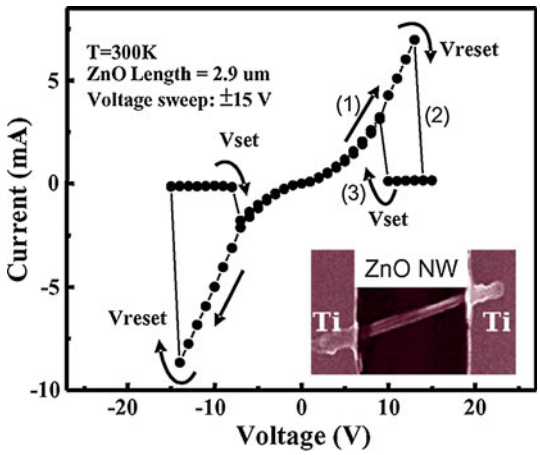

Fig. 23 *I–V* switching characteristics of a single ZnO-NW memory. *Inset* shows the test structure having two Ti contacts [334]

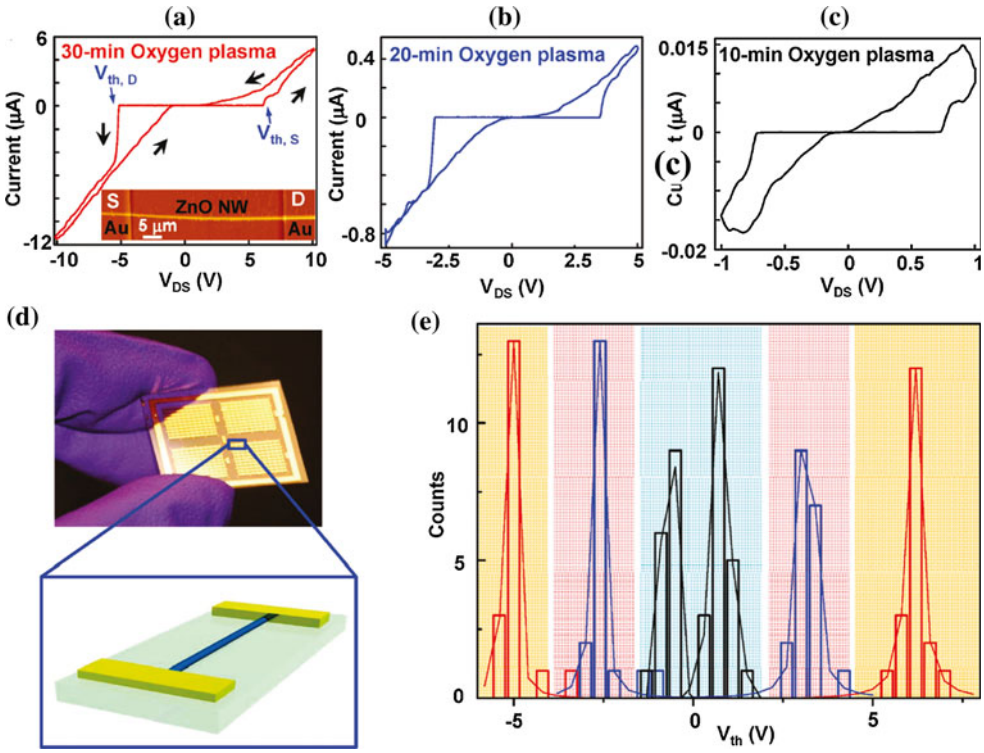

Fig. 24 Effects of oxygen plasma treatment on electrical properties of ZnO PRRAM cells. **a–c** *I–V* characteristics of ZnO PRRAM cells after 30-, 20-, and 10-min oxygen plasma treatment, respectively (sweeping frequency is 0.1 Hz). *Inset* of **a** shows the AFM image of a ZnO PRRAM cell. **d** Optical image of the large-scale as-fabricated PRRAM cells after printing transfer of ZnO-NWs and patterning of metal electrodes. **e** Statistical distributions of the $V_{th,S}$ and $V_{th,D}$ peaks for PRRAM cells with different periods of oxygen plasma treatment. *Red*, *blue*, and *black lines* are for PRRAM cells with 30, 20, and 10 min oxygen plasma treatment, respectively [336] (Color figure online)

bias, PRRAM cell switched back to OFF state. RS observed for a single PRRAM cell is independent of the polarity of the voltage which indicates unipolar switching [337]. *I–V* characteristic of the PRRAM cell was different from those studied in previous single ZnO-NW-based piezotronic devices [336, 338, 339].

Figure 24a–c shows the *I–V* curve of the oxygen plasma-treated sample for 30, 20, and 10 min, respectively, and the samples were compared with Ar plasma treatment. Considerable changes have been observed in the shape, threshold voltage, and current of the *I–V* curves for these samples. With the increase of oxygen plasma treatment time, threshold voltage of the PRRAM cell and hysteresis increased accordingly, as shown in Fig. 24a–c. However, threshold voltage has been decreased and the conductance increased with respect to the pristine one and finally rectification disappeared in the *I–V* curve of PRRAM cell after argon plasma treatment, due to the influence of oxygen vacancies on Schottky contacts between ZnO and metal electrodes [340]. Sharp and distinct statistical distributions of the $V_{th,S}$ and $V_{th,D}$ peaks for PRRAM cells with different periods of oxygen plasma treatment are observed, as shown in Fig. 24e. Small dissimilarity and asymmetry observed between $V_{th,S}$ and $V_{th,D}$ within each group of PRRAM cells are due to the nonuniform geometry of ZnO-NWs, as indicated by the AFM image of inset in Fig. 24a. Non-Boolean neuromorphic computing might also be comprehended by integrating arrays of high-density resistive memory cells [341, 342] on flexible substrates.

Most of the reports demonstrate typical RS behavior of 1D-ZnO nanostructures from the limited controlling conditions. Recently, Park et al. [343] introduced photons as an alternative stimulus for activating RS behaviors of hydrothermally grown ZnO-NRs on FTO glass. Prior to ZnO-NRs growth, ZnO seed layer was deposited by rf magnetron sputtering. Evaporated Au was used as a top electrode. The RS behavior in light and dark conditions was compared to describe how RS memories were beneficial from photons. A significant change in the resistance states has been reported for the Au/ZnO-NRs/FTO structures [343].

RS was derived by both electrical stimulus and photon modulation. RS attributed to filament annihilation and generation was intimately connected to the conditions relating to oxygen vacancies dissipation and reappearance caused by chemisorbed oxygen species deficient on the ZnO-NRs surfaces under various photo-illumination conditions. ZnO-NRs can be used as a model system to exhibit photo-stimulated RS in high-surface-area nanomaterials, in which photo-driven surface states strongly affect their photoconductivity and resistance states [343]. This proposal may extend the applications of RRAM in photonic devices, including photodiodes, photodetectors, and photoenergy devices.

RS in doped nanostructures

Yang et al. [344] demonstrated RS behavior in the single Sb-doped ZnO nanobelt/SiO_x/p-Si(001) device, measured by AFM. However, direct contact between top and bottom

electrodes may cause a short circuit issue if the top electrode is prepared on ZnO-NRs RS film with a low packing density. A hybrid RS device consists of ZnO-NRs embedded in insulating poly-methyl-methacrylate (PMMA) polymer that can evade such direct contact [345]. But, embedding ZnO-NRs in PMMA is a time consuming and complex technique.

Yao et al. [346] investigated the bipolar RS behavior, and conduction mechanisms of gallium-doped ZnO (GZO) NR thin films on Au/Ti/SiO_2/p-Si(001) substrates. Prior to the growth of GZO-NRs [Ga/Zn molar ratios: 0 % (device-1), 6 % (device-2), 8 % (device-3), and 10 % (device-4)] by aqueous solution method at 90 °C, a 79.30 ± 1.54-nm-thick ZnO buffer layer was first deposited on Au/Ti/SiO_2/p-Si(001) substrate by rf magnetron sputtering. Figure 25a shows the negative voltage set/reset process of the 10 % GZO-NR-based memory devices. ±0.9 V set voltage is required with I_C of 15 mA to swift the device from HRS to LRS. Opposite voltage sweeping (V_{OFF} ~ ±0.8 V) creates abrupt decrease in current as the device switches from LRS to HRS again. Devices show only bipolar RS behaviors from both sides, as shown in Fig. 25a, b. Device yield as shown in Fig. 25c signifies that the devices with compact GZO-NR thin films (devices-3 and 4) accomplish higher device yield (more than 55 %) than the device with porous GZO-NR thin films (device-2).

Among the various proposed models for RS mechanisms, conducting filament formation/rupture successfully explained the bipolar RS behavior of NRs-based RS memory structures. Figure 26a plots the dependences of resistance value of ON and OFF states on pattern size of RRAM structures having GZO-NR active layer [346]. R_{ON} and R_{OFF} seem to be independent of the pattern size. Therefore, the formation/rupture of localized conducting filaments is the preferred switching mechanism of the Au/GZO-NR/ZnO/Au devices. According to the filamentary model, localized conducting filaments consist of defects such as oxygen vacancies between top and bottom electrodes, leading to transition from OFF to ON state [326, 328, 329, 347–349].

Similarity in ionic radii between Ga^{3+} (0.62 Å) and Zn^{2+} (0.74 Å) suggests that the gallium ion can substitute the zinc ion. Possible defect equations of this substitution can be expressed as:

$$Ga_2O_3 \xrightarrow{ZnO} 2Ga_{Zn}^{\bullet} + 3O_o^x + V_{Zn}^{//}, \quad (7)$$

$$ZnO + O_o^x \Leftrightarrow V_{Zn}^{//} + 2V_O^{\bullet} + \frac{1}{2}O_2(g) + ZnO \quad (\text{surface}), \quad (8)$$

$$ZnO \Leftrightarrow V_{Zn}^{//} + V_O^{\bullet\bullet} + ZnO \quad (\text{surface}), \quad (9)$$

$$O_o^x \Leftrightarrow \frac{1}{2}O_2(g) + V_O^{\bullet} + e^{/}, \quad (10)$$

$$O_o^x \Leftrightarrow \frac{1}{2}O_2(g) + V_O^{\bullet\bullet} + 2e^{/}. \quad (11)$$

where $Ga_{Zn}^{\bullet}$ denotes the gallium ion with a single positive charge in zinc site, the $V_o^{\bullet}$ and $V_o^{\bullet\bullet}$ are the oxygen vacancies with single and double positive charges, respectively, O_o^x indicates the neutral oxygen ion in lattice site, $V_{Zn}^{//}$ is the zinc vacancy with double negative charge, and $e^{/}$ denotes the electron with a single negative charge for compensation. According to Eq. (7), incorporating Ga into the ZnO-NRs generates ionic defects ($V_{Zn}^{//}$) associated with a Zn^{2+}

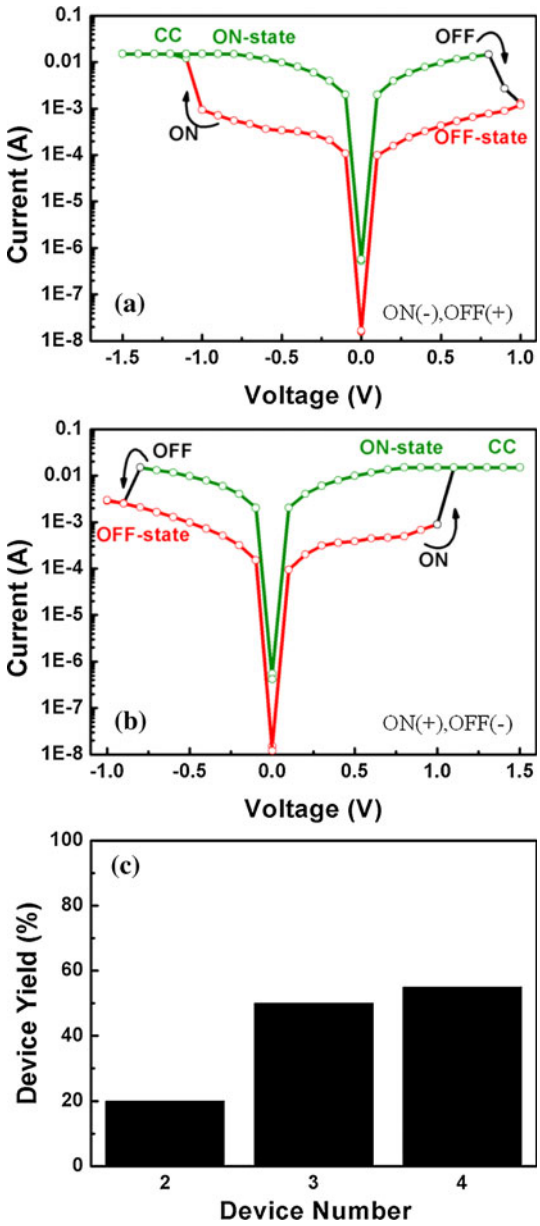

Fig. 25 **a**, **b** Typical bipolar *I–V* switching curve of 10 % Ga-doped ZnO-NRs-based RRAM. **c** Device yield of the device-2, 3, and 4, respectively [346]

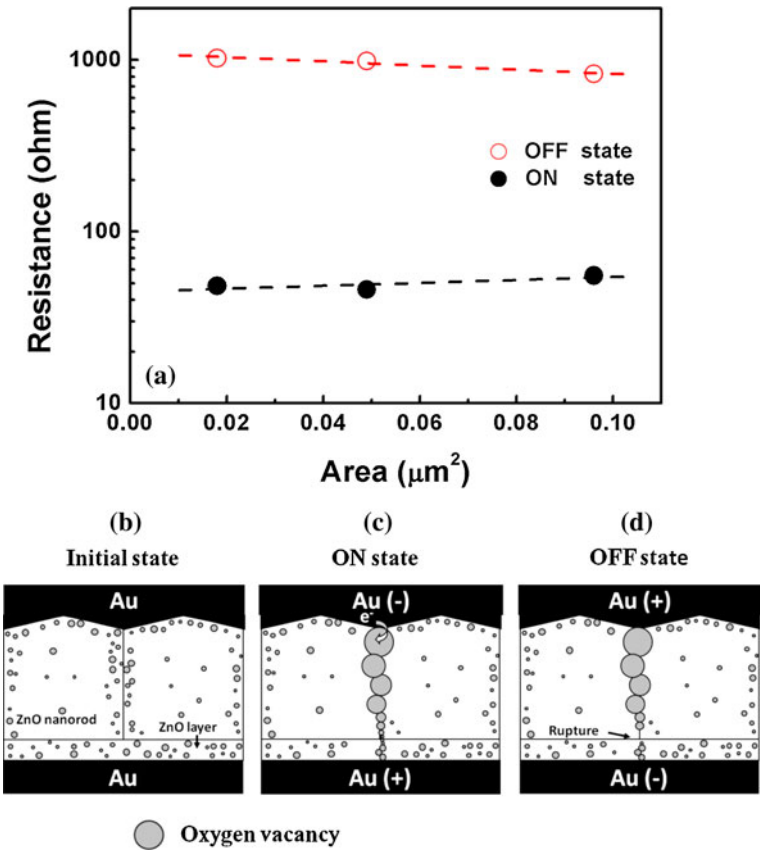

Fig. 26 **a** Pattern size dependence of the resistance value in ON and OFF states. **b–d** Schematic diagrams of bipolar RS mechanism of GZO NR film devices through the formation/rupture of conducting filaments formed between GZO NR side wall and ZnO seed layer [346]

site substituted by a Ga^{3+} ion. Furthermore, the generated defects change the equilibrium of the system. Based on Eqs. (8)–(11) and Le Chatelier principle [349], system tends to shift in the direction that reduces the change in conditions (i.e., reactions shift toward left-hand side as oxygen vacancies are reduced). As a result, both $V_{Zn}^{//}$ and $e^{/}$ suppress the formation of oxygen vacancies as the Ga/Zn molar ratios in the NRs increase.

Defects mobility at the film surface is substantially higher than that in the single-crystal material (Fig. 26b) [346], which suggest that oxygen vacancies with single ($V_o^{\bullet}$) and double positive charges ($V_o^{\bullet\bullet}$) can easily assemble to form conducting filaments at the surface of the single-crystalline GZO-NR. By applying negative voltage, many positive ionic defects of $V_o^{\bullet\bullet}$ or $V_o^{\bullet}$ are supposed to accumulate and form conducting filaments at GZO-NRs (grain boundary) surface. Injected electrons are simultaneously transported from top of the bottom electrode and the device is switched from HRS to LRS (Fig. 26c). Applying a positive voltage on top electrode, V_{OFF} releases the positive ionic defects of $V_o^{\bullet\bullet}$ or $V_o^{\bullet}$ at the weakest region (between the interface of GZO-NR and ZnO seed layer) and conducting filament is ruptured at the interface. The device returns back to HRS again (Fig. 26d). By applying a negative voltage to V_{ON} $V_o^{\bullet\bullet}$ or $V_o^{\bullet}$ is re-assembled and conducting filaments are formed and the device switched back to LRS again (Fig. 26c) [346, 347].

Table 2 shows a comparison of RS memory device structures and their switching parameters for different 1D-ZnO nanostructures-based RRAM devices. The devices with the lowest operational voltage for bipolar 1D-ZnO-NRs-based RRAM devices were those having transparent FTO or ITO bottom electrodes and Pt top electrodes [331, 343]. Switching parameters of our 1D-GZO-NRs-based bipolar RRAM device are also comparable in every respect with others [346].

Future trends of ZnO 1D nanostructures

Technical and scientific potentials of 1D nanostructures are enormous, and future of this sub-field of nanoscience is unquestionably bright. Outstanding progress has been observed in recent years on the synthesis of 1D-ZnO nanostructures, and it attains a huge attention for its extraordinary properties and versatile applications. Improvement in electron transport applying these nanostructures is a reality, and current densities have been improved when modifying the NRs tip. We believe that scalable, low-cost, and improved nanoelectronic, display,

Table 2 Comparison of RS parameters of 1D-ZnO-based RRAM devices

Device structure	Pt/ZnO-NR/ITO	Cu/ZnO-NW/Pd	Cu/ZnO-NW/Pd	Au/ZnO-PNW/Au	Au/ZnO-NR/FTO	Single Sb:ZnO nanobelt/SiO_x/p-Si	ZnO-NR/PMMA	Au/Ga-ZnO/Au
V_F (V)	ND	22	1–3	ND	ND	ND	ND	No
Switching type	Bipolar	Unipolar	Bipolar	Unipolar	Bipolar	Bipolar	Bipolar	Bipolar
V_{reset} (V)	−0.6	±12	~−1.6	5	−0.6	2.2	−1.5	±0.8
V_{set} (V)	0.7	±7	≤3	5.73	0.7	6	2	±0.9
$R_{off/on}$	7	7.7×10^5	$>10^5$	10^5	10	ND	ND	>10
Set/reset speed	ND	ND	ND	ND	ND	ND	ND	1 μs
Cycles	120	100	7	ND	ND	ND	200	100
Retention (s)	10^3	ND	$>2 \times 10^6$	ND	ND	ND	ND	ND
Reference	[331]	[334]	[335]	[336]	[343]	[344]	[345]	[346]

V_F forming voltage, $R_{off/on}$ resistance ratio between HRS and LRS, *ND* no data available

sensor, and photonic devices using 1D-ZnO nanostructures could be possibly soon marketed commercially.

One of the versatile and easiest methods that has been used to grow ZnO nanostructures is hydrothermal techniques with the possibility of large-scale production, but reproducibility of the nanostructure is still a challenge. Templates- or nanolithography-based synthesis methods provide the opportunity of reproducibility and the control of nanostructure in height and diameter. A general tendency seems to be toward the application of nanofabrication synthesis techniques, but the selected method must be simple enough to circumvent or ease multi-step processes or need for special equipment for the fabrication of 1D-ZnO nanostructures.

NVM have generated an increasing interest for their advantages such as low operating power, faster access time, larger retention and cycling, scalability over traditional flash, and their large variety of applications in modern microprocessor-based devices such as cars, computers, note books, etc. As the device scaling down researchers are looking for different combinations for low power, flexible, transparent, 3D NVM devices; RRAM devices based on vertically aligned 1D-ZnO nanostructures may reach the goal of NVM technologies in the near future. We hope that flexible transparent RRAM using 1D-ZnO nanostructures could be more attractive in the near future. Due to the various applications of 1D-ZnO nanostructures, it may be quite ahead in the race between different metal oxides in the semiconductor industry for interdisciplinary applications.

Conclusions

A comprehensive review of properties, processing, and device applications of 1D-ZnO nanostructures is presented. ZnO has been a subject of varying degrees of research effort over the decades not only for their amazing advantageous chemical and physical properties, but also for their current and future electronic device applications. Different synthesis techniques including chemical sol–gel, MOCVD, vapor-phase transport, sputtering, evaporation, PLD, and hydrothermal are commonly used to grow 1D-ZnO nanostructures on different substrates including glass, Si, or polymer. Templates are also used to achieve well-aligned, distributed, and tunable NRs/NWs. Morphologies of the grown NWs, nanotubes, nanopagoda, etc., and their tip morphologies are studied using FESEM and TEM. Development in the optical properties of ZnO-1D nanostructures using PL study is briefly reviewed. Using PL the role of oxygen vacancies in the optical properties is presented. An application of ZnO-1D NW in field effect transistor is described. Improvement of field emission properties of different 1D-ZnO nanostructures by modifying the morphology of nanostructures to nanoneedle, nanotip, nanopagoda, etc., is briefly reviewed. Sensing properties and mechanisms of 1D-ZnO nanostructures in the form of aligned nanotubes, NWs, mesh of NWs, etc., are presented. Applications involved in biosensor, PH sensor, etc., are also briefly reviewed. Applications of ZnO-1D nanostructures in heterojunction and homojunction LED and photodetector are also presented. ZnO is also used as a laser diode for its large exciton binding energy (60 meV) and wide band gap (3.37 eV) which could lead to lasing action based on exciton recombination even above room temperature. It attracted a huge interest for the applications in emerging NVM. RS properties of ZnO-NRs and single NW increased their technological importance. Effect of Ga doping in ZnO-NRs on RS properties is also briefly discussed. This review provides a roadmap of ZnO-1D nanostructures for sensors, LED, photodetector, laser, and NVM device applications.

Research highlights

- Recent progress of the synthesis and applications of ZnO 1D nanostructures.
- Structural and electro-optical properties of ZnO 1D nanostructures are reviewed.
- Sensing properties of doped ZnO 1D nanostructures are studied.
- Applications as LEDs and photodetector are briefly discussed.
- RS of Ga-doped and undoped ZnO-NRs are briefly studied.

Acknowledgements This work is supported by National Science Council, Taiwan under Grant No NSC-100-2811-E-009-026 and NSC-99-2221-E-009-166-MY3.

References

Data collections like INSPEC or Web of Science gives more than 15000 references for ZnO nanostructures. Evidently we can give in the following only a very limited selection, which cannot include even all relevant papers. In many cases we are also unable to address every cited paper individually but consider them as suggestions for "further reading" for those interested in more details. We apologize for this shortcoming.

1. Liang WY, Yoffe AD (1968) Phys Rev Lett 20:59
2. Jin BJ, Im S, Lee SY (2000) Thin Solid Films 366:107
3. Huang MH, Mao S, Feick H, Yan H, Wu Y, Kind H, Weber E, Russo R, Yang P (2001) Science 292:1897
4. Ryu YR, Zhu S, Budai JD, Chandrasekhar HR, Miceli PF, White HW (2000) J Appl Phys 88:201
5. Shan FK, Shin BC, Kim SC, Yu YS (2004) J Eur Ceram Soc 24:1861
6. Bunn CW (1935) Proc Phys Soc Lond 47:835
7. Damen TC, Porto SPS, Tell B (1966) Phys Rev 142:570
8. Galli G, Coker JE (1970) Appl Phys Lett 16:439
9. Mead CA (1965) Phys Lett 18:218
10. Brillson LJ (1978) J Vac Sci Technol 15:1378
11. Brown HE (1957) Zinc oxide discovery. The New Jersey Zinc Company, New York
12. Brown HE (1976) Zinc oxide properties and applications. The New Jersey Zinc Company, New York
13. Miller PH Jr (1950) In: Henisch HK (ed) Proceedings of the international conference on semiconductor materials, Reading. Butterworth Scientific, London, p 172
14. Heiland H, Mollwo E, Stöckmann F (1959) Solid State Phys 8:191
15. Mandal S, Singha RK, Dhar A, Ray SK (2008) Mater Res Bull 43:244
16. Wei A, Sun XW, Wang JX (2006) Appl Phys Lett 89:123902
17. Zhao ZW, Chen XJ, Tay BK, Chen JS, Han ZJ, Khor KA (2007) Biosens Bioelectron 23:135
18. Klingshirn C (2007) Phys Status Solidi B 244:3027
19. Pan ZW, Dai ZR, Wang ZL (2001) Science 291:1947
20. Wang ZL (2004) J Phys: Condens Matter 16:R829
21. Wang ZL (2007) Appl Phys A 88:7
22. Kukreja LM, Misra P, Fallert J, Sartor J, Kalt H, Klingshirn C (2008) 2008 IEEE photonics global @Singapore IPGC 1
23. Willander M, Nur O, Zhao QX, Yang LL, Lorenz M, Cao BQ, Zúñiga Pérez J, Czekalla C, Zimmermann G, Grundmann M, Bakin A, Behrends A, Al-Suleiman M, El-Shaer A, Mofor AC, Postels B, Waag A, Boukos N, Travlos A, Kwack HS, Guinard J, Dang DLS (2009) Nanotechnology 20:332001
24. Wang ZL, Song J (2006) Science 312:242
25. Yichun L, Mingya Z, Guiye S, Yajun L, Baiqu H, Guoliang Y (2008) J Phys Chem B 112:6484
26. Al-Hilli SM, Al-Mofarji RT, Willander M (2006) Appl Phys Lett 89:173119
27. Sadik PW, Pearton SJ, Norton DP, Lambers E, Ren F (2007) J Appl Phys 101:104514
28. Wang ZL (2007) Mater Today 10:20
29. Ronning C, Gao PX, Ding Y, Wang ZL, Schwen D (2004) Appl Phys Lett 84:783
30. Qingyu X, Hartmann L, Shengqiang Z, Mcklich A, Helm M, Biehne G, Hochmuth H, Lorenz M, Grundmann M, Schmidt H (2008) Phys Rev Lett 101:076601
31. Yi GC, Wang C, Park W II (2005) Semicond Sci Technol 20:s22
32. Cho S, Jeong H, Park DH, Jung SH, Kim HJ, Lee KH (2010) Cryst Eng Commun 12:968
33. Kang DS, Han SK, Kim JH, Yang SM, Kim JG, Hong SK, Kim D, Kim H (2009) J Vac Sci Technol B 27:1667
34. Hsueh TJ, Chen YW, Chang SJ, Wang SF, Hsu CL, Lin YR, Lin TS, Chen IC (2007) J Electrochem Soc 154:J393
35. Ra HW, Choi DH, Kim SH, Im YH (2009) J Phys Chem C 113:3512
36. Wang X, Summers CJ, Wang ZL (2004) Nano Lett 4:423
37. Panigrahi S, Basak D (2011) Nanoscale 3:23362341
38. Liu DF, Xiang YJ, Liao Q, Zhang JP, Zhang ZX, Liu LF, Ma WJ, Shen J, Zhou WY, Xie SS (2007) Nanotechnology 18:405303
39. Wei Y, Dong Y, Li C, Xu S, Ryo JH, Dupuis R, Sood AK, Polla DL, Wang ZL (2008) J Phys Chem C 112:18935
40. Lao CS, Liu J, Gao P, Zhang L, Davidovic D, Tummala R, Wang ZL (2006) Nano Lett 6:263
41. Liu B, Zeng HC (2009) Nano Res 2:201
42. Han J, Fan F, Xu C, Lin S, Wei M, Duan X, Wang ZL (2010) Nanotechnology 21:405203
43. Gao PX, Ding Y, Wang ZL (2009) Nano Lett 9:137
44. Gao H, Zhang X, Zhou M, Zhou E, Zhang E, Zhang Z (2006) Solid state Commun 140:455
45. Hughes WL, Wang ZL (2005) Appl Phys Lett 86:043106
46. Kong XY, Ding Y, Yang R, Wang ZL (2004) Science 303:1348
47. Xing YJ, Xi ZH, Zhang XD, Song JH, Wang RM (2005) Appl Phys A 80:1527
48. Zhang YS, Wang LS, Liu X, Yan YJ, Chen CQ, Zhu J (2005) J Phys Chem B 109:13091
49. Lv H, Sang DD, Li HD, Du XB, Li DM, Zou GT (2010) Nanoscale Res Lett 5:620
50. Calestani D, Zha MZ, Zanotti L, Villani M, Zappettini A (2011) Cryst Eng Commun 13:1707
51. Park WI, Kim DH, Jung SW, Yi GC (2002) Appl Phys Lett 80:4232
52. Park W, Yi GC (2004) Adv Mater 16:87
53. Ishikawa Y, Shimizu Y, Sasaki T, Koshizaki N (2006) J Colloid Interface Sci 300:612
54. He H, Cai W, Lin Y, Chen B (2010) Langmuir 26:8925
55. Zhao Y, Uk Kwon Y (2004) Chem Lett 33:1578
56. Liu B, Zeng HC (2003) J Am Chem Soc 125:4430
57. Akhavan O, Mehrabian M, Mirabbaszadeh K, Azimirad R (2009) J Phys D 42:225305
58. Guo M, Diao P, Cai S (2005) Appl Surf Sci 249:71

59. Park SK, Park JH, Ko KY, Yoon S, Chu KS, Kim W, Do YR (2009) Cryst Growth Des 9:3615
60. Chander R, Raychaudhuri AK (2008) Solid State Commun 145:81
61. Iijima S, Ichihashi T (1993) Nature 363:603
62. Xu S, Qin Y, Wei Y, Yang RY, Wang ZL (2010) Nat Nanotech 5:366
63. Wang B, Zhu LF, Yang YH, Xu NS, Yang GW (2008) J Phys Chem C 112:6643
64. Heer WA, Chatelain A, Ugarte D (1995) Science 270:1179
65. Soci C, Zhang A, Bao XY, Kim H, Wang D (2010) J Nanosci Nanotechnol 10:1
66. Pauporte T, Lincot D (1999) Appl Phys Lett 75:3817
67. Levy-Clement C, Tena-Zaera R, Ryan MA, Katty A, Hodes G (2005) Adv Mater 17:1512
68. Tena-Zaera R, Katty A, Bastide S, Levy-Clement C, O'Regan B, Munoz-Sanjose V (2005) Thin Solid Films 483:372
69. Guo M, Yang CY, Zhang M, Zhang Y-J, Ma T, Wang X-D, Wang X-D (2008) Electrochim Acta 53:4633
70. Chen Z, Gao L (2006) J Cryst Growth 293:522
71. Wang Z, Qian ZF, Yin J, Zhu ZK (2004) Langmuir 20:3441
72. Li Q, Kumar V, Li Y, Zhang H, Mark JT, Chang RPH (2005) Chem Mater 17:1001
73. Yao I-C, Lin P, Huang S-H, Tseng T-Y (2012) IEEE Trans Compon Packag Manuf Technol 2:1143
74. Wong MH, Berenov A, Qi X, Kappers MJ, Barber ZH, Llly B, Lockman Z, Ryan MP, Macmanus-Driscoll JL (2003) Nanotechnology 14:968
75. Wang Q, Wang G, Jie J, Han X, Hou JG (2005) Thin Solid Films 492:61
76. Yang LL, Zhao QX, Willander M (2009) J Alloys Compd 469:623
77. Yao I-C, Lin P, Tseng T-Y (2009) Nanotechnology 20:125202
78. Yao I-C, Lin P, Tseng T-Y (2012) IEEE Trans Nanotechnol 11:746
79. Sandan VE, Rogers DJ, Tehrani FH, McClintock R, Razeghi M, Drouhin H-J, Clochard MC, Sallet V, Garry G, Fayoud F (2008) Proc SPIE-Int Soc Opt Eng 6895:68950Z
80. Zhang G, Nakamura A, Aoki T, Temmyo J, Matsui Y (2006) Appl Phys Lett 89:113112
81. Kim S-W, Fujita S, Fujita S (2005) Appl Phys Lett 86:153119
82. Ye ZZ, Xu WZ, Zhou J, Wang ZL (2007) Solid State Commun 41:464
83. Kim HW, Kim HM, Shim J-H, Cho N-H, Lee C (2005) J Mater Sci: Mater Electron 16:13
84. Liu SM, Gu SL, Zhu SM, Ye JD, Liu W, Zhou X, Zhang R, Shi Y, Zheng YD (2007) J Cryst Growth 299:303
85. Kim S-W, Fujita S, Fujita S (2002) Appl Phys Lett 81:5036
86. Muthukumar S, Sheng H, Zhong J, Zhang Z, Emanetoglu NW, Lu Y-C (2003) IEEE Trans Nanotechnol 2:50
87. Kim S-W, Fujita S, Fujita S (2002) Jpn J Appl Phys 41:L543
88. Wu J-J, Liu S-C (2002) Adv Mater 14:215
89. Yuan H, Zhang Y (2004) J Cryst Growth 263:119
90. Lee W, Jeong M-C, Myoung J-M (2004) Acta Mater 52:3949
91. Montenegro DN, Souissi A, Martínez-Tomás C, Muñoz-Sanjosé V, Sallet V (2012) J Cryst Growth 359:122
92. Jeong M-C, Oh B-Y, Lee W, Myoung J-M (2004) J Cryst Growth 268:149
93. Baxter JB, Aydil ES (2005) J Cryst Growth 274:407
94. Park WI, Yi G-C, Kim M, Pennycook SJ (2002) Adv Mater 14:1841
95. Pasquier AD, Chen H, Lu Y (2006) Appl Phys Lett 89:253513
96. Yin M, Gu Y, Kuskovsky IL, Andelman T, Zhu Y, Neumark GF, O'Brien S (2004) J Am Chem Soc 126:6206
97. Gu Y, Kuskovsky Igor L, Yin M, O'Brien S, Neumark GF (2004) Appl Phys Lett 85:3833
98. Gargas DJ, Gao H, Wang H, Yang P (2011) Nano Lett 11:3792
99. Wagner RS, Ellis WC (1964) Appl Phys Lett 4:89
100. Scharowski E (1953) Z Phys 135:318
101. Li S, Zhang X, Yan B, Yu T (2009) Nanotechnology 20:495604
102. Grabowska J, Nanda KK, McGlynn E, Mosnier J-P, Henry MO (2005) Surf Coat Technol 200:1093
103. Huang MH, Wu Y, Feick H, Tran N, Weber E, Yang P (2001) Adv Mater 13:113
104. Li SY, Lee CY, Tseng T-Y (2003) J Cryst Growth 247:357
105. Yang RS, Wang ZL (2007) Phil Mag 87:2097
106. Willander M, Nur O, Bano N, Sultana K (2009) New J Phys 11:125020
107. Mandal S, Sambasivarao K, Dhar A, Ray SK (2009) J Appl Phys 106:024103
108. Saunders RB, Garry S, Byrne D, Henry MO, McGlynn E (2012) Cryst Growth Des 12:5972
109. Hung NL, Ahn E, Park S, Jung H, Kim H, Hong S-K, Kim D, Hwang C (2009) J Vac Sci Technol A 27:1347
110. Choopun S, Hongsith N, Tanunchai S, Chairuangsri T, Krua-in C, Singkarat S, Vilaithong T, Mangkorntong P, Mangkorntong N (2005) J Cryst Growth 282:365
111. Kim S, Jeong M-C, Oh B-Y, Lee W, Myoung J-M (2006) J Cryst Growth 290:485
112. Heo YW, Varadarajan V, Kaufman M, Kim K, Norton DP, Ren F, Fleming PH (2002) Appl Phys Lett 81:3046
113. Kang BS, Heo YW, Tien LC, Norton DP, Ren F, Gila BP, Pearton SJ (2005) Appl Phys A 80:1029
114. Wang HT, Kang BS, Ren F, Tien LC, Sadik PW, Norton DP, Pearton SJ, Lin J (2005) Appl Phys Lett 86:243503
115. Yao BD, Chan YF, Wang N (2002) Appl Phys Lett 81:757
116. Kong YC, Yu DP, Zhang B, Fang W, Feng SQ (2001) Appl Phys Lett 78:407
117. Choopun S, Tabata H, Kawai T (2005) J Cryst Growth 274: 167
118. Zhang Y, Russo RE, Mao SS (2005) Appl Phys Lett 87:133115
119. Zhai T, Gu Z, Ma Y, Yang W, Zhao L, Yao J (2006) Mater Chem Phys 100:281
120. Zhai T, Gu Z, Dong Y, Zhong H, Ma Y, Fu H, Li Y, Yao J (2007) J Phys Chem C 111:11604
121. Lin L, Zhain T, Bando Y, Golberg D (2012) Nano Energy 1:91
122. Xu X, Fang X, Zeng H, Zhai T, Bando Y, Golberg D (2010) Sci Adv Mater 2:273
123. Zhao L, Yang W, Luo Y, Zhai T, Zhang G, Yao J (2005) Chem Eur J 11:3773
124. Li L, Pan S, Dou X, Zhu Y, Huang X, Yang Y, Li G, Zhang L (2007) J Phys Chem C 111:7288
125. Zeng H, Xu X, Bando Y, Gautam UK, Zhai T, Fang X, Liu B, Golberg D (2009) Adv Funct Mater 19:3165
126. Li L, Zhai T, Zeng H, Fang X, Bando Y, Golberg D (2011) J Mater Chem 21:40
127. Maiti UN, Nandy S, Karan S, Mallik B, Chattopadhyay KK (2008) Appl Surf Sci 254:7266
128. Tam KH, Cheung CK, Leung YH, Djurisic AB, Ling CC, Beling CD, Fung S, Kwok WM, Chan WK, Phillips DL, Ding L, Ge WK (2006) J Phys Chem B 110:20865
129. Ma T, Guo M, Zhang M, Zhang YJ, Wang XD (2007) Nanotechnology 18:035605
130. Chen S-W, Wu J-M (2011) Acta Mater 59:841
131. Djurisic AB, Leung YH (2006) Small 2:944
132. Lin K-F, Cheng H-M, Hsu H-C, Hsieh W-F (2006) Appl Phys Lett 88:263117
133. Djurišić AB, Ng AMC, Chen XY (2010) Prog Quantum Electron 34:191
134. Voss T, Bekeny C, Wischmeier L, Gafsi H, Borner S, Schade W, Mofor AC, Bakin A, Waag A (2006) Appl Phys Lett 89:182107
135. Yang P, Yan H, Mao S, Russo R, Johnson J, Saykally R, Morris N, Pham J, He R, Choi H-J (2002) Adv Funct Mater 12:323

136. Jie J, Wang G, Chen Y, Han X, Wang Q, Xu B, Hou JG (2005) Appl Phys Lett 86:031909
137. Ozaki S, Tsuchiya T, Inokuchi Y, Adachi S (2005) Phys Status Solidi A 202:1325
138. Zhang BP, Binh NT, Segawa Y, Kawashiba Y, Haga K (2004) Appl Phys Lett 84:586
139. Wischmeier L, Voss T, Ruckmann I, Gutowski J (2008) Nanotechnology 19:135705
140. Robin IC, Lafossas M, Garcia J, Rosina M, Latu-Romain E, Ferret P, Gilet P, Tchelnokov A, Azize M, Eymery J, Feuillet G (2009) Microelectron J 40:250
141. Subannajui K, Wongchoosuk C, Ramgir N, Wang C, Yang Y, Hartel A, Cimalla V, Zacharias M (2012) J Appl Phys 112:034311
142. Göpel W, Pollmann J, Ivanov I, Reihl B (1982) Phys Rev B 26:3144
143. Reynolds DC, Look DC, Jogai B, Litton CW, Collins TC, Harsch W, Cantwell G (1998) Phys Rev B 57:12151
144. Zhang XT, Liu YC, Zhi ZZ, Zhang JY, Lu YM, Shen DZ, Xu W, Fan XW, Kong XG (2002) J Lumin 99:149
145. Hamby DW, Lucca DA, Klopfstein MJ, Cantwell G (2003) J Appl Phys 93:3214
146. Alves H, Pfisterer D, Zeuner A, Riemann T, Christen J, Hofmann DM, Meyer BK (2003) Opt Mater 23:33
147. Reynolds DC, Look DC, Jogai B, Litton CW, Collins TC, Harsch H, Cantwell G (2001) Appl Phys Lett 79:3794
148. Leung YH, Kwok WM, Djurisic AB, Phillips DL, Chan WK (2005) Nanotechnology 16:579
149. Johnson JC, Knutsen KP, Yan H, Law M, Zhang Y, Yang P, Saykally RJ (2004) Nano Lett 4:197
150. Song JK, Willer U, Szarko JM, Leone SR, Li S, Zhao Y (2008) J Phys Chem C 112:1679
151. Zhao QX, Yang LL, Willander M, Semelius BE, Holtz PO (2008) J Appl Phys 104:073526
152. Lettieri S, Amato LS, Maddalena P, Comini E, Baratto C, Todros S (2009) Nanotechnology 20:175706
153. Richters J-P, Wischmeier L, Ruckmann I, Gutowski J, Voss T (2009) Phys Status Solidi C 6:560
154. Kwok WM, Djurisic AB, Leung YH, Chan WK, Phillips DL (2005) Appl Phys Lett 87:223111
155. Han X, Wang G, Wang Q, Cao L, Liu R, Zou B, Hou JG (2005) Appl Phys Lett 86:223106
156. Hong S, Joo T, Park WI, Jun YH, Yi G-C (2003) Appl Phys Lett 83:4157
157. Robin IC, Gauron B, Ferret P, Tavares C, Feuillet G, Dang LS, Gayral B, Gerard JM (2007) Appl Phys Lett 91:143120
158. Sönmez E, Meral K (2012) J Nanomater, Article ID 957035
159. Chang P, Fan Z, Tseng W, Wang D, Chiou W, Hong J, Lu JG (2004) Chem Mater 16:5133
160. Chik H, Liang J, Cloutier SG, Kouklin N, Xu JM (2004) Appl Phys Lett 84:3376
161. Liu CH, Yiu WC, Au FCK, Ding JX, Lee CS, Lee ST (2003) Appl Phys Lett 83:3168
162. Li QH, Wan Q, Liang YX, Wang TH (2004) Appl Phys Lett 84:4556
163. Heo YW, Tien LC, Norton DP, Kang BS, Ren F, Gila BP, Pearton SJ (2004) Appl Phys Lett 85:2002
164. Arnold MS, Avouris P, Pan ZW, Wang ZL (2003) J Phys Chem B 107:659
165. Park WI, Kim JS, Yi G-C, Bae MH, Lee H-J (2004) Appl Phys Lett 85:5052
166. Erhart P, Albe K, Klein A (2006) Phys Rev B 73:205203
167. Fan Z, Lu JG (2005) Appl Phys Lett 86:03211
168. Chang P-C, Fan Z, Chien C-J, Stichtenoth D, Ronning C, Lu JG (2006) Appl Phys Lett 89:133113
169. Hossain FM, Nishii J, Takagi S, Sugihara T, Ohtomo A, Fukumura T, Koinuma H, Ohno H, Kawasaki M (2004) Phys E 21:911
170. Yuan GD, Zhang WJ, Jie JS, Fan X, Zapien JA, Leung YH, Luo LB, Wang PF, Lee CS, Lee ST (2008) Nano Lett 8:2591
171. Joseph M, Tabata H, Saeki H, Ueda K, Kawai T (2001) Phys B 302:140
172. Xiang B, Wang P-W, Zhang X-Z, Dayeh SA, Aplin DPR, Soci C, Yu D, Wang D (2007) Nano Lett 7:323
173. Brauer G, Anwand W, Grambole D, Skorupa W, Hou Y, Andreev A, Teichert C, Tam KH, Djurišić AB (2007) Nanotechnology 18:195301
174. Ra HW, Im YH (2008) Nanotechnology 19:485710
175. Chiu S-P, Lin Y-H, Lin J-J (2009) Nanotechnology 20:015203
176. Hu Y, Liu Y, Li W, Gao M, Liang X, Li Q, Peng L-M (2009) Adv Funct Mater 19:2380
177. Rakhshani AE (2008) Semicond Sci Technol 23:075037
178. Kim K, Kang H, Lee JS, Kim S, Kang W, Kim G-T (2009) Appl Phys A 94:253
179. Mridha S, Basak D (2009) Nanotechnology 20:075203
180. He JH, Ho CH (2007) Appl Phys Lett 91:233105
181. Banerjee D, Jo SH, Ren ZF (2004) Adv Mater 16:2028
182. Xing YJ, Xi ZH, Xue ZQ, Zhang XD, Song JH, Wang RM, Xu J, Song Y, Zhang SL, Yu DP (2003) Appl Phys Lett 83:1689
183. Tseng Y-K, Huang C-J, Cheng H-M, Lin I-N, Liu K-S, Chen I-C (2003) Adv Funct Mater 13:811
184. Zhu YW, Zhang HZ, Sun XC, Feng SQ, Xu J, Zhao Q, Xiang B, Wang RM, Yu DP (2003) Appl Phys Lett 83:144
185. Zhang HZ, Wang RM, Zhu YW (2004) J Appl Phys 96:624
186. Li YB, Bando Y, Golberg D (2004) Appl Phys Lett 84:3603
187. Xu CX, Sun XW (2003) Appl Phys Lett 83:3806
188. Jo SH, Banerjee D, Ren ZF (2004) Appl Phys Lett 85:1407
189. Kim TY, Kim JY, Lee SH, Shim HW, Lee SH, Suh EK, Nahm KS (2004) Synth Met 144:61
190. Filip V, Nicolaescu D, Tanemura M, Okuyama F (2001) Ultramicroscopy 89:39
191. Charbonnier FM, Mackie WA, Hartman RL, Xie TB (2001) J Vac Sci Technol B 19:1064
192. Liu JP, Xu CX, Zhu GP, Cui YP, Yang Y, Sun XW (2007) J Phys D 40:1906
193. Lee CJ, Lee TJ, Lyu SC, Zhang Y, Ruh H, Lee HJ (2002) Appl Phys Lett 81:3648
194. Lee CY, Tseng T-Y, Li SY, Lin P (2006) Nanotechnology 17:83
195. Xi Y, Hu CG, Han XY, Xiong YF, Gao PX, Liu GB (2007) Solid State Commun 141:506
196. Yang JH, Liu GM, Lu J, Qiu YF, Yang SH (2007) Appl Phys Lett 90:103109
197. Wang JX, Sun XW, Yang Y, Huang H, Lee YC, Tan OK, Vayssieres L (2006) Nanotechnology 17:4995
198. Manekkathodi A, Lu MY, Wang CW, Chen LJ (2010) Adv Mater 22:4059
199. Xu S, Ding Y, Wei YG, Fang H, Shen Y, Sood AK, Polla DL, Wang ZL (2009) J Am Chem Soc 131:6670
200. Gao P, Wang ZZ, Liu KH, Xu Z, Wang WL, Bai XD, Wang EG (2009) J Mater Chem 19:1002
201. Sun K, Jing Y, Park N, Li C, Bando Y, Wang DL (2010) J Am Chem Soc 132:15465
202. Liu X, Lin P, Yan X, Kang Z, Zhao Y, Lei Y, Li C, Du H, Zhang Y (2013) Sens Actuator B 176:22
203. Liu TY, Liao HC, Lin CC, Hu SH, Chen SY (2006) Langmuir 22:5804
204. Liu NS, Fang GJ, Zeng W, Long H, Yuan LY, Zhao XZ (2011) J Phys Chem C 115:570
205. Kwon SS, Hong WK, Jo G, Maeng J, Kim TW, Song S, Lee T (2008) Adv Mater 20:4557

206. Wei TY, Yeh PH, Lu SY, Wang ZL (2009) J Am Chem Soc 131:17690
207. Yeh PH, Li Z, Wang ZL (2009) Adv Mater 21:4975
208. Zhou J, Gu YD, Hu YF, Mai WJ, Yeh PH, Bao G, Sood AK, Polla DL, Wang ZL (2009) Appl Phys Lett 94:191103
209. Wei TY, Huang CT, Hansen BJ, Lin YF, Chen LJ, Lu SY, Wang ZL (2010) Appl Phys Lett 96:013508
210. Tang HX, Yan M, Zhang H, Li SZ, Ma XF, Wang M, Yang D (2006) Sens Actuator B 114:910
211. Barr TL (1978) J Phys Chem 82:1801
212. Esser P, Gopel W (1980) Surf Sci 97:309
213. Chang JF, Kuo HH, Leu IC, Hon MH (2002) Sens Actuator B 84:258
214. Rao GS, Trivikrama, Rao D, Tarakarama (1999) Sens Actuator B 55:166
215. Lamb DA, Irvine SJC (2004) J Cryst Growth 273:111
216. Mridha S, Basak D (2006) Semicond Sci Technol 21:928
217. Bie L-J, Yan X-N, Yin J, Duan Y-Q, Yuan Z-H (2007) Sens Actuator B 126:604
218. Hsueh T-J, Hsu C-L, Chang S-J, Chen I-C (2007) Sens Actuator B 126:473
219. Wan Q, Li QH, Chen YJ, Wang TH, He XL, Li JP, Lin CL (2004) Appl Phys Lett 84:3654
220. Xu J, Chen Y, Li Y, Shen J (2005) J Mater Sci 40:2919. doi: 10.1007/s10853-005-2435-4
221. Wang C, Chu X, Wu M (2006) Sens Actuator B 113:320
222. Lupan O, Ursaki VV, Chai G, Chow L, Emelchenko GA, Tiginyanu IM, Gruzintsev AN, Redkin AN (2010) Sens Actuator B 144:56
223. Parthangal PM, Cavicchi RE, Zachariah MR (2006) Nanotechology 17:3786
224. Tien LC, Sadik PW, Norton DP, Voss LF, Pearton SJ, Wang HT, Kang BS, Ren F, Jun J, Lin J (2005) Appl Phys Lett 87:222106
225. Sun Z-P, Liu L, Zhang L, Jia D-Z (2006) Nanotechnology 17:2266
226. Rout CS, Hari Krishna S, Vivekchand SRC, Govindaraj A, Rao CNR (2006) Chem Phys Lett 418:586
227. Liao L, Lu HB, Li JC, Liu C, Fu DJ, Liu YL (2007) Appl Phys Lett 91:173110
228. Shalish I, Temkin H, Narayanamurti V (2004) Phys Rev B 69:245401
229. Lettieri S, Bismuto A, Maddalena P, Baratto C, Comini E, Faglia G, Sberveglieri G, Zanotti L (2006) J Non-Cryst Solids 352:1457
230. Comini E, Baratto C, Faglia G, Ferroni M, Sberveglieri G (2007) J Phys D 40:7255
231. Zhu XL, Yuri I, Gan X, Suzuki I, Li GX (2007) Biosens Bioelectron 22:1600
232. Zhang FF, Wang XL, Ai SY, Sun ZD, Wan Q, Zhu ZQ, Xian YZ, Jin LT, Yamamoto K (2004) Anal Chim Acta 519:155
233. Singh SP, Arya SK, Pandey P, Malhotra BD, Saha S, Sreenivas K, Gupta V (2007) Appl Phys Lett 91:6390
234. Arya SK, Saha S, Ramirez-Vick JE, Gupta V, Bhansali S, Singh SP (2012) Anal Chim Acta 737:1
235. Wang JX, Sun XW, Wei A, Lei Y, Cai XP, Li CM, Dong ZL (2006) Appl Phys Lett 88:233106
236. Zang JF, Li CM, Cui XQ, Wang JX, Sun XW, Dong H, Sun CQ (2007) Electroanalysis 19:1008
237. Yang K, She GW, Wang H, Ou XM, Zhang XH, Lee CS, Lee ST (2009) J Phys Chem C 113:20169
238. Sun XW, Wang JX, Wei A (2008) J Mater Sci Technol 24:649
239. Topoglidis E, Cass AEG, Regan BO, Durrant JR (2001) J Electroanal Chem 517:20
240. Kong T, Chen Y, Ye Y, Zhang K, Wang Z-X, Wang X-P (2009) Sens Actuator B 138:344
241. Wang J, Li S, Zhang Y (2010) Electrochim Acta 55:4436
242. Asif MH, Usman Ali SM, Nur O, Willander M, Brännmark C, Strålfors P, Englund UH, Elinder F, Danielsson B (2010) Biosens Bioelectron 25:2205
243. Al-Hilli SM, Willander M, Ost M, Stralfors A (2007) J Appl Phys 102:084304
244. Chang SP, Li CW, Chen KJ, Chang SJ, Hsu CL, Hsueh TJ, Hsueh HT (2012) Sci Adv Mater 4:1174
245. Zhou J, Xu NS, Wang ZL (2006) Adv Mater 18:2432
246. Li Z, Yang RS, Yu M, Bai F, Li C, Wang ZL (2008) J Phys Chem C 112:20114
247. Sheng X, Wang ZL (2011) Nano Res 4:1013
248. Kim KK, Lee SD, Kim H, Park JC, Lee SN, Park Y, Park SJ, Kim SW (2009) Appl Phys Lett 94:071118
249. Yang Y, Sun XW, Tay BK, You GF, Tan ST, Teo KL (2008) Appl Phys Lett 93:253107
250. Wong C-Y, Lai L-M, Leung S-L, Roy VAL, Pun EY-B (2008) Appl Phys Lett 93:023502
251. Zhang JY, Li PJ, Sun H, Shen X, Deng TS, Zhu KT, Zhang QF, Wei JL (2008) Appl Phys Lett 93:021116
252. Lai E, Kim W, Yang PD (2008) Nano Res 1:123
253. Jeong M-C, Oh B-Y, Ham M-H, Lee SW, Myong JM (2007) Small 3:568
254. Sun M, Zhang QF, Sun H, Zhang J, Wu JL (2009) J Vac Sci Technol B 27:618
255. Sun H, Zhang Q-F, Wu J-L (2006) Nanotechnology 17:2271
256. Ling B, Sun XW, Zhao JL, Tan ST, Dong ZL, Yang Y, Yu HL, Qi KC (2008) Phys E 41:635
257. Kim DC, Han WS, Cho HK, Kong BH, Kim HS (2007) Appl Phys Lett 91:231901
258. Yang W, Huo HB, Dai L, Ma RM, Liu SF, Ran GZ, Shen B, Lin CL, Qin GG (2006) Nanotechnology 17:4868
259. Willander M, Zhao QX, Hu QH, Klason P, Kuzmin V, Al. Hilli SM, Nur O, Lozovik YE (2008) Superlattices Microstruct 43:352
260. Sun XW, Huang JZ, Wang JX, Xu Z (2008) Nano Lett 8:1219
261. Könenkamp R, Word RC, Godinez M (2005) Nano Lett 5:2005
262. Könenkamp R, Word RC, Schlegel C (2004) Appl Phys Lett 85:6004
263. Wadeasa A, Beegum SL, Raja S, Nur O, Willander M (2009) Appl Phys A 95:807
264. Lee CY, Hui YY, Su WF, Lin CF (2008) Appl Phys Lett 92:261107
265. Lee CY, Huang YT, Su WF, Lin CF (2006) Appl Phys Lett 89:231116
266. Liu JP, Qu SC, Zeng XB, Xu Y, Gou XF, Wang ZJ, Zhou HY, Wang ZG (2007) Appl Surf Sci 253:7506
267. Wadeasa A, Nur O, Willander M (2009) Nanotechnology. 20:065710
268. Rout CS, Rao CNR (2008) Nanotechnology 19:285203
269. Guo H, Zhou J, Lin Z (2008) Electrochem Commun 10:146
270. Ng AMC, Djurišić AB, Tam KH, Kwok WM, Chan WK, Tam WY, Phillips DL, Cheah KW (2008) Adv Funct Mater 18:566
271. Lee SD, Kim YS, Yi MS, Choi JY, Kim SW (2009) J Phys Chem C 113:8954
272. Zhang L, Li Q, Dong Y, Huang R, Zhang Z, Zhao F (2012) J Opt 14:125601
273. Park SH, Kim SH, Han SW (2007) Nanotechnology 18:055608
274. Jha SK, Luan C, To CH, Kutsay O, Kováč J, Zapien JA, Bello I, Lee ST (2012) Appl Phys Lett 101:211116
275. Jeong MC, Oh BY, Ham MH, Myoung JM (2006) Appl Phys Lett 88:202105
276. Guo R, Nishimura J, Matsumoto M, Higashihata M, Nakamura D, Okada T (2009) Appl Phys B 94:33
277. An SJ (2012) Appl Phys Lett 100:23115
278. An SJ, Yi GC (2007) Appl Phys Lett 91:123109

279. Yoo CHJ, Hong YJ, Cho J, Kim YJ, Jeon SR, Baek JH, Yi GC (2009) Appl Phys Lett 94:213101
280. Ng AMC, Xi YY, Hsu YF, Djurišić AB, Chan WK, Gwo S, Tam HL, Cheah KW, Fong PWK, Lui HF, Surya C (2009) Nanotechnology 20:445201
281. Sun M, Zhang QF, Wu JL (2007) J Phys D 40:3798
282. Hsu YF, Xi YY, Tam KH, Djurišić AB, Luo J, Ling CC, Cheung CK, Ng AMC, Chan WK, Deng X, Beling CD, Fung S, Cheah KW, Fong PWK, Surya CC (2008) Adv Funct Mater 18:1020
283. Amin G, Sandberg MO, Zainelabdin A, Zaman S, Nur O, Willander M (2012) J Mater Sci 47:4726. doi:10.1007/s10853-012-6342-1
284. Amin G, Zaman S, Zainelabdin A, Nur O, Willander M (2011) Phys Status Solidi RRL 5(2):71
285. Jin Y, Wang J, Sun B, Blakesley JC, Greenham NC (2008) Nano Lett 8:1649
286. Yao IC, Lin P, Tseng TY (2012) Sens Actuators A 178:26
287. Keem K, Kim H, Kim G, Lee J, Min B, Cho K, Sung M, Kim S (2004) Appl Phys Lett 84:4376
288. Soci C, Zhang A, Xiang B, Dayeh SA, Aplin DPR, Park J, Bao XY, Lo YH, Wang D (2007) Nano Lett 7:1003
289. Wilson DH, Hoyt S, Janata J, Booksh K, Obando L (2001) IEEE Sens 1:256
290. He JH, Ke J, Chang PH, Tsai KT, Yang PC, Chan IM (2012) Nanoscale 4:3399
291. Wang H, Baek S, Song J, Lee J, Lim S (2008) Nanotechnology 19:075607
292. Yen W, Mechau N, Hahn H, Krupke R (2010) Nanotechnology 21:115501
293. Chantarat N, Chen WY, Chen SY, Lin CC (2009) Nanotechnology 20:395201
294. Cheng J, Zhang Y, Guo R (2008) J Cryst Growth 310:57
295. Lin CC, Lin WH, Li YYJ (2009) Nanosci Nanotechnol 9:2813
296. Ates ES, Kucukyildiz S, Unalan HE (2012) ACS Appl Mater Interfaces 4:5142
297. Li Y, Dong X, Cheng C, Zhou X, Zhang P, Gao J, Zhang H (2009) Phys B 404:4282
298. Park D, Yong K (2008) J Vac Sci Technol B 26:1933
299. Ghosh R, Basak D (2007) Appl Phys Lett 90:243106
300. Hsueh TJ, Hsu CL, Chang SJ, Lin YR, Chang SP, Chiou YZ, Lin TS, Chen IC (2007) IEEE Trans Nanotechnol 6:595
301. Rajabi M, Dariani RS, Iraji ZA (2012) Sens Actuators A 180:11
302. Law JBK, Thong JTL (2006) Appl Phys Lett 88:133114
303. Hsu CL, Hsueh TJ, Chang SP (2008) J Electrochem Soc 155:K59
304. Cheng G, Li ZH, Wang SJ, Gong HC, Cheng K, Jiang XH, Zhou SM, Du ZL, Cui T, Zou GT (2008) Appl Phys Lett 93:123103
305. Fan Z, Dutta D, Chien CJ, Chen HY, Brown EC, Chang PC, Lu JG (2006) Appl Phys Lett 89:213110
306. Ha R, Pyun JC, Oh H, Choi HJ (2008) J Korean Phys Soc 53:1992
307. Kim W, Chu KS (2009) Phys Status Solidi A 206:179
308. Huang H, Fang G, Mo X, Yuan L, Zhou H, Wang M, Xiao H, Zhao X (2009) Appl Phys Lett 94:06351
309. Guo Z, Zhao D, Liu Y, Shen D, Zhang J, Li B (2008) Appl Phys Lett 93:163501
310. ul Hasan K, Nur O, Willander M (2012) Appl Phys Lett 100:211104
311. Cao H, Xu JY, Zhang DZ, Chang SH, Ho ST, Seelig EW, Liu X, Chang RPH (2000) Phys Rev Lett 84:5584
312. Bagnall DM, Chen YF, Zhu ZQ, Yao T, Koyama S, Shen MY, Goto T (1997) Appl Phys Lett 70:2230
313. Yu P, Tang ZK, Wang GKL, Kawasaki M, Ohtomo A, Koinuma H, Segawa Y (1998) J Cryst Growth 184:601
314. Klingshirn C (1992) J Cryst Growth 117:753
315. Johnson JC, Yan H, Yang P, Saykally RJ (2003) J Phys Chem 107:8816
316. Panda D, Maikap S, Dhar A, Ray SK (2009) Electrochem Solid-State Lett 12:H7
317. Panda D, Dhar A, Ray SK (2009) Semicond Sci Technol 24:115020
318. Tseng TY, Nalwa HS (2009) Handbook of nanoceramics and their based nanodevices, vol. 4: electronic applications. American Scientific, Valencia
319. Ray SK, Panda D, Aluguri R (2012) iFirst: 1
320. Inoue IH, Yasuda S, Akinaga H, Takagi H (2008) Phys Rev B 77:035105
321. Tseng TY, Sze SM (2012) Nonvolatile memories materials, devices and applications, vol 1 and 2. American Scientific, Valencia
322. Wang SY, Tseng TY (2011) J Adv Dielectr 1:141
323. Panda D, Dhar A, Ray SK (2012) IEEE Trans Nanotechnol 11:51
324. Panda D, Dhar A, Ray SK (2010) J Appl Phys 108:104513
325. Lee DY, Tseng TY (2011) J Appl Phys 110:114117
326. Panda D, Huang CY, Tseng TY (2012) Appl Phys Lett 100:112901
327. Rahaman SZ, Maikap S, Chen WS, Lee HY, Chen FT, Kao MJ, Tsai MJ (2012) Appl Phys Lett 101:073106
328. Lee DY, Tseng TY (2012) IEEE Electron Dev Lett 33:803
329. Wu MC, Lin YW, Jang WY, Lin CH, Tseng TY (2011) IEEE Electron Dev Lett 32:1026
330. Wu MC, Jang WY, Lin CH, Tseng TY (2012) Semicond Sci Technol 27:065010
331. Chang WY, Lin CA, He JH, Wu TB (2010) Appl Phys Lett 96:242109
332. Guan W, Long S, Liu Q, Liu M, Wang W (2008) IEEE Electron Dev Lett 29:434
333. Liu Q, Dou C, Wang Y, Long S, Wang W, Liu M, Zhang M, Chen J (2009) Appl Phys Lett 95:023501
334. Chiang YD, Chang WY, Ho CY, Chen CY, Ho CH, Lin SJ, Wu TB, He JH (2012) IEEE Trans Electron Dev 58:1735
335. Yang Y, Zhang X, Gao M, Zeng F, Zhou W, Xie S, Pan F (2011) Nanoscale 3:1917
336. Wu WZ, Wang Z (2011) Nano Lett 11:2779
337. Waser R, Dittmann R, Staikov G, Szot K (2009) Adv Mater 21:2632
338. Wang ZL (2010) Nano Today 5:540
339. Wu WZ, Wei YG, Wang ZL (2010) Adv Mater 22:4711
340. Allen MW, Durbin SM (2008) Appl Phys Lett 92:12210
341. Boahen K (2005) Sci Am 295:56
342. Jo SH, Chang T, Ebong I, Bhadviya BB, Mazumder P, Lu W (2010) Nano Lett 10:1297
343. Park J, Lee S, Yong K (2012) Nanotechnology 23:385707
344. Yang Y, Qi J, Guo W, Zin Z, Zhang Y (2012) Appl Phys Lett 96:093107
345. Tseng ZL, Kao PC, Shih FM, Huang HH, Wang JY, Chu SY (2010) Appl Phys Lett 97:212103
346. Yao IC, Lee DY, Tseng TY, Lin P (2012) Nanotechnology 23:145201
347. Panda D, Tseng TY (2013) Thin Solid Films 531:1
348. Lin CY, Tu BC, Lin CC, Lin CH, Tseng TY (2006) IEEE Electron Dev Lett 27:725
349. Zumdahl SS (1998) Chemical principle, 3rd edn. Houghton Mifflin, New York